RSC Advances

PAPER

View Article Online
View Journal | View Issue

Cite this: *RSC Adv.*, 2023, **13**, 34534

A synergistic investigation of azo-thiazole derivatives incorporating thiazole moieties: a comprehensive exploration of their synthesis, characterization, computational insights, solvatochromism, and multimodal biological activity assessment†

Dara Muhammed Aziz, *[a] Sangar Ali Hassan, [a] Alla Ahmad M. Amin,[a] Media Noori Abdullah, [b] Karzan Qurbani[c] and Shujahadeen B. Aziz[d]

In the present study, a novel series of azo-thiazole derivatives (**3a–c**) containing a thiazole moiety was successfully synthesized. The structure of these derivatives was examined by spectroscopic techniques, including ^{1}H NMR, ^{13}C NMR, FT-IR, and HRMS. Further, the novel synthesized compounds were evaluated for their *in vitro* biological activities, such as antibacterial and anti-inflammatory activities, and an *in silico* study was performed. The antibacterial results demonstrated that compounds **3a** and **3c** (MIC = 10 μg mL^{-1}) have a notable potency against *Staphylococcus aureus* compared to azithromycin (MIC = 40 μg mL^{-1}). Alternatively, compound **3b** displayed a four-fold higher potency (24 recovery days, 1.83 mg day^{-1}) than Hamazine (28 recovery days, 4.14 mg day^{-1}) in promoting burn wound healing, and it also exhibited a comparable inhibitory activity against screened bacterial pathogens compared to the reference drug. Docking on 1KZN, considering the excellent impact of compounds on the crystal structure of *E. coli* 1KZN, a 24 kDa domain, in complex with clorobiocin, indicated the close binding of compounds **3a–c** with the active site of the 1KZN protein, which is consistent with their observed biological activity. Additionally, we conducted molecular dynamics simulations on the docked complexes of compounds **3a–c** with 1KZN retrieved from the PDB to assess their stability and molecular interactions. Furthermore, we assessed their electrochemical characteristics *via* DFT calculations. Employing PASS and pkCSM platforms, we gained insights into controlling the bioactivity and physicochemical features of these compounds, highlighting their potential as new active agents.

Received 22nd September 2023
Accepted 30th October 2023

DOI: 10.1039/d3ra06469g

rsc.li/rsc-advances

1 Introduction

The field of drug discovery has witnessed significant advances that are driven by two primary approaches: the pursuit of novel proteins as drug targets and the optimization of clinical drugs. Modern drug discovery relies on novel protein identification and targeting.[1] Advancements in genomics, proteomics, and structural biology have uncovered unexplored areas in the human proteome. Moreover, optimizing clinical drugs by using data from trials and post-marketing surveillance improves their safety, efficacy, and delivery methods.[2–5] Drug repurposing involves reusing known drugs for new therapies, thus enhancing their clinical value. Advances in pharmaceutical chemistry and drug delivery give rise to extended-release formulations, boosting patient compliance and treatment efficacy.[6–9] Recently, bacterial and inflammatory infections have given rise to diverse and serious diseases. Thus, the discovery of novel antibacterial and anti-inflammatory agents holds promise for mitigating these medical challenges. In recent times, medicinal chemistry research has focused on the development of innovative antimicrobial agents, distinguished by their novel structural designs and molecular targets. A pressing concern for healthcare professionals in the foreseeable future is the escalating prevalence of multidrug-resistant pathogenic bacteria, which swiftly develop resistance to commonly utilized

[a]*Department of Chemistry, College of Sciences, University of Raparin, Kurdistan Regional Government, Main Street, Ranyah 46012, Iraq. E-mail: darachem@uor.edu.krd*

[b]*Department of Chemistry, College of Science, Salahaddin University, Erbil 44002, Iraq*

[c]*Department of Biology, College of Sciences, University of Raparin, Kurdistan Regional Government, Main Street, Ranyah 46012, Iraq*

[d]*Advanced Polymeric Materials Research Lab, Department of Physics, College of Science, University of Sulaimani, Kurdistan Regional Government, Qlyasan Street, Sulaimani, 46001, Iraq*

† Electronic supplementary information (ESI) available. See DOI: https://doi.org/10.1039/d3ra06469g

antibiotics for the treatment of human infections.[10–12] Thiazole, a pivotal heterocycle, plays a key role in potent biologically active molecules, such as sulfathiazole (an antimicrobial), ritonavir (an antiretroviral), abafungin (an antifungal), bleomycin (a neoplastic agent), and tiazofurin (a neoplastic agent).[13] Thiazole and its derivatives have found wide applications in the medical field, addressing various conditions, such as hypertension, inflammation, schizophrenia, bacterial infections, and HIV infections.[14–18] Additionally, they have been utilized as antagonists of fibrinogen receptors, displaying antithrombotic characteristics, and as inhibitors of bacterial DNA gyrase B.[19,20] Thiazole frameworks, exemplified by dasatinib and dabrafenib, are known for their potent antitumor effects.[21,22] Azo-thiazole refers to a class of organic compounds that contain both an azo group (N=N) and a thiazole ring in their molecular structure.[23] This unique combination of functional groups contributes to the distinct properties and potential applications of this compound in various fields. However, although heterocyclic compounds containing azo groups have a substantial presence in pharmaceuticals and the development of therapeutic agents, the related literature remains somewhat limited.[24–26] In current scientific investigations, there has been a noticeable increase in attention directed towards producing heterocyclic compounds that integrate azo groups and their related derivatives. This increase is attributed to their notable biological actions, which encompass a wide spectrum of powerful influences including antimicrobial, antifungal, antiviral, anticonvulsant, antidiabetic, anti-inflammatory, antitubercular, DNA binding for anticancer uses, analgesic characteristics, and their potential for chemical sensing activities.[27,28] The molecular hybridization approach represents an effective and frequently employed strategy in contemporary medicinal chemistry research for developing and advancing novel therapeutic agents.[29–31] Considering previously reported results, we opted to develop some new hybrid structures incorporating azo-thiazole in various thiazole ring systems through an acetamide linkage. This combination was proposed in an effort to investigate the impact of this hybridization and structural diversity on the anticipated antibacterial efficacy. Our aim was to introduce greater biological relevance to the compounds of interest. The final synthesized compounds in this study, *i.e.*, azo-thiazole-bearing benzamide thiazole derivatives, were subjected to *in vitro* antibacterial and *in vivo* anti-inflammatory and acute toxicity measurements. Moreover, we conducted molecular docking, molecular dynamic simulation and ADME studies.

2 Experimental

2.1. Materials and reagent

All compounds were directly obtained from SIGMA-ALDRICH (UK) and used as received with no further purification. The melting points of the synthesized substances were measured using an uncorrected Bio Core melting point device equipped with open capillaries. The progress of the reactions was observed *via* thin-layer chromatography (TLC) on aluminum sheets coated with silica gel 60 F254. The mobile phase consisted of ethyl acetate and diethyl ether in a 1 : 1 ratio, and detection was accomplished under UV light. FT-IR spectra were recorded using a Thermo Scientific Nicolet iS50 series FT-IR spectrometer. Spectral information was collected using a JENWAY UV/vis 6705 series single-beam UV/vis scanning spectrophotometer. ^{1}H and ^{13}C NMR spectroscopy was conducted using a BRUKER AVANCE 500 MHz NMR spectrometer with DMSO-d_6 as the solvent. Chemical shifts were recorded in ppm relative to the Me4Si internal standard, and J values were expressed in Hz. High-resolution mass spectrometry (HRMS) data were acquired using an Agilent LC/MSD TOF mass spectrometer.

2.2. Synthesis method

2.2.1. Synthesis of azo compound (3). Thiazol-2-amine (6.4 g, 64 mmol) was dissolved in a 300 mL glass beaker containing 37% w/v HCl (20 mL, 96 mmol) and distilled water (20 mL). The resulting solution was chilled in an ice bath to reach a temperature in the range of 0 °C to 5 °C. Concurrently, $NaNO_2$ (5 g, 70.4 mmol) was dissolved in 24 mL of distilled water, and also cooled using an ice bath. A thiazole-2-diazonium chloride salt solution was prepared by gradually introducing the $NaNO_2$ solution in the thiazol-2-amine solution while stirring, ensuring that the temperature was controlled in the range of 0 °C to 5 °C. The obtained solution was maintained in the temperature range of 0 °C to 5 °C for a specific period. In a distinct procedure, a solution containing 2-hydroxybenzoic acid (10 g, 64 mmol) dissolved in 30 mL of a 10% w/v KOH solution was also cooled to 0 °C to 5 °C using an ice bath. The solution containing potassium 2-carboxyphenolate was slowly added with constant stirring to the thiazole-2-diazonium chloride solution until a gel-like substance developed. Subsequently, 60 mL of cold water was incorporated. The mixture was left stirring at room temperature overnight. The resulting compound was collected through filtration, and then subjected to recrystallization from a mixture containing ethanol and water in a 7 : 3 proportion. After characterization, the final product was obtained as a yellow-colored powder.[32]

2.2.1.1. 2-Hydroxy-5-(thiazol-2-yldiazenyl)benzoic acid (3). Light brown solid, yield 93.52%, m.p. 129–130 °C. IR cm^{-1}: 3232.05 (OH), 3007.34 (Csp^2–H aromatic), 1655.58 (C=O), 1609.95 (C=C aromatic); 1580.33 (–N=N–), and 852.34 (aromatic substituted). ^{1}H NMR (DMSO-d_6, δ ppm): 6.70–6.72 (1H, d, Ar–H), 7.16–7.18 (1H, d, Ar–H), 7.52 (1H, s, Ar–H), 8.04–8.05 (1H, d, thiazole-H), 8.34–8.35 (1H, d, thiazole-H), 12.26 (1H, s, 1H, s, OH, D_2O exchangeable), 12.99 (1H, s, Ar–COOH). ^{13}C NMR (DMSO-d_6, δ ppm): 113.36, 117.56, 119.65, 123.00, 128.0, 130.74, 136.13, 143.74, 161.62, 172.42. HRMS (ESI) (cal.): $C_{10}H_7N_3O_3S$ $[M + H]^+$, m/z: 249.02 (100.0%), 250.02 (11.9%), 251.02 (4.5%); (found): 249.0277 (100.0%), 250.0147 (11.9%), 251.0016 (4.5%), 252.0040 (1.1%).

2.2.2. Synthesis of azo-amide derivatives (3a–c). A three-neck 250 mL round-bottom flask, previously dried using a flame, was secured with two glass stoppers. The arrangement was comprised of a vacuum-jacketed Dean–Stark trap linked to a reflux condenser featuring a nitrogen inlet, in addition to a Teflon-coated magnetic stirring bar. In the reaction container,

2-hydroxy-5-(thiazol-2-yldiazenyl)benzoic acid (2.46 g, 15 mmol), boric acid (0.010 g, 0.15 mmol), and 50 mL of toluene were added. The stirred mixture, showing a distinct hue, was then swiftly mixed with amines (**a–c**) (15.5 mmol) simultaneously. Subsequently, the obtained reaction mixture was refluxed for a duration of 16 h, resulting in the accumulation of around 0.3 mL of water in the Dean–Stark trap. Following the cooling of the mixture to ambient temperature, it was poured with agitation into 250 mL of hexanes, leading to the immediate generation of a white solid precipitate. Stirring was continued for an extra 30 min, after which the precipitate was filtered under suction through a sintered glass filter funnel. Next, the gathered solid was successively rinsed with two 30 mL quantities of hexanes, followed by two 30 mL quantities of distilled water. Subsequently, the solid was subjected to vacuum drying at room temperature for a duration of 12 h, resulting in the formation of the target products (**3a–c**).[33]

*2.2.2.1. 2-Hydroxy-N-(thiazol-2-yl)-5-(thiazol-2-yldiazenyl) benzamide (**3a**).* Gray solid, yield 77.11%, m.p. 125–126 °C, IR cm^{-1}: 3232.75 (OH), 3006.51 (Csp^2–H aromatic), 1655.05 (C=O), 1608.99 (C=C aromatic); 1578.76 (–N=N–), and 852.00 (aromatic substituted); ^1H NMR (DMSO-d_6, δ ppm): 4.14 (1H, s, 1H, s, OH, D_2O exchangeable), 6.95–6.97 (1H, d, Ar–H), 7.17–7.19 (1H, d, Ar–H), 7.53 (1H, s, Ar–H), 7.80–7.82 (1H, d, CH-thiazole), 7.92–7.94 (1H, d, CH-thiazole). 8.00–8.02 (1H, d, CH-thiazole), 8.24–8.26 (1H, d, CH-thiazole), 11.52 (1H, s, NH, D_2O exchangeable). ^{13}C NMR (DMSO-d_6, δ ppm): 115.09, 119.51, 123.08, 127.95, 129.65, 138.88, 143.79, 144.48, 147.10, 164.90, 166.06, 171.33, 176.74. HRMS (ESI) (cal.): $C_{13}H_9N_5O_2S_2$ $[M + H]^+$, *m*/*z*: 331.02 (100.0%), 332.02 (18.4%), 333.02 (1.3%), 334.02 (1.6%); (found): 331.0276 (100.0%), 332.0137 (14.1%), 333.0173 (8.9%), 334.01298 (1.2%).

*2.2.2.2. N-(Benzo[d]thiazol-2-yl)-2-hydroxy-5-(thiazol-2-yldiazenyl)benzamide (**3b**).* Reddish-brown solid, yield 61.38%, m.p. 70–71 °C, IR cm^{-1}: 3116.83.05 (OH), 3090.68 (Csp^2–H aromatic), 1668.25 (C=O), 1603.12 (C=C aromatic); 1578.42 (–N=N–), and 833.98 (aromatic substituted); ^1H NMR (DMSO-d_6, δ ppm): 4.16 (s, H_{14}, OH), 6.96–6.98 (1H, d, Ar–H), 7.20–7.21 (1H, d, Ar–H), 7.42 (1H, s, Ar–H), 7.53–7.55 (1H, d, CH-thiazole), 7.82–7.84 (1H, d, Ar–H), 7.93–7.95 (1H, d, Ar–H), 8.04–8.06 (1H, d, CH-thiazole), 8.13–8.15 (1H, d, Ar–H), 8.47–7.49 (1H, d, Ar–H), 11.30 (1H, s, NH, D_2O exchangeable). ^{13}C NMR (DMSO-d_6, δ ppm): 114.93, 117.57, 119.48, 119.69, 123.19, 127.89, 129.77, 143.07, 143.91, 144.53, 149.45, 155.59, 158.04, 165.74, 169.57, 171.40, 176.69. HRMS (ESI) (cal.): $C_{17}H_{11}N_5O_2S_2$ $[M + H]^+$, *m*/*z*: 381.04 (100.0%), 382.04 (18.4%), 383.09 (9.0%), 384.02 (1.7%); (found): 381.0443 (100.0%), 382.0350 (18.4%), 383.0258 (8.9%), 384.0166 (1.6%).

*2.2.2.3. 2-Hydroxy-5-(thiazol-2-yldiazenyl)-N-(4-(thiazol-2-ylsulfonyl)phenyl)benzamide (**3c**).* Brown solid, yield 70.06%, m.p. 90–91 °C, IR cm^{-1}: 3116.31 (OH), 3090.60 (Csp^2–H aromatic), 1668.16 (C=O), 1603.41 (C=C aromatic); 1578.20 (–N=N–) and 833.91 (aromatic substituted); ^1H NMR (DMSO-d_6, δ ppm): 6.58–6.61 (1H, d, Ar–H), 6.83–6.84–7.21 (1 H, d, Ar–H), 6.94 (1H, s, Ar–H), 6.98–7.00 (1H, d, Ar–H), 7.18–7.21 (1H, d, CH-thiazole), 7.53–7.56 (1H, d, CH-thiazole), 7.79–7.82 (1H, d, Ar–H), 7.92–7.95 (1H, d, Ar–H), 10.63 (1H, s, NH, D_2O exchangeable), 11.96 (1H, s, OH, D_2O exchangeable). ^{13}C NMR (DMSO-d_6, δ ppm): 114.93, 117.57, 119.48, 119.69, 123.19, 127.89, 129.77, 143.05, 143.91, 144.53, 149.45, 155.59, 158.04, 165.74, 169.57, 171.40, 176.69. HRMS (ESI) (cal.): for $C_{19}H_{13}N_5O_4S_3$ $[M + H]^+$, *m*/*z*: 471.01 (100.0%), 472.02 (20.5%), 473.01 (13.6%), 474.01 (2.8%); (found): 471.0228 (100.0%), 472.0130 (20.5%), 473.0086 (13.3%), 474.0128 (2.7%).

2.3. Biological study

2.3.1. Antibacterial activity. The antibacterial activity of synthetic compounds **3** and **3a–c** was assessed *in vitro* using Gram-positive bacteria including *Bacillus cereus*, *Staphylococcus aureus*, *Staphylococcus epidermidis*, and *Pseudomonas aeruginosa*, as well as Gram-negative bacteria including *Shigella* sp., *Escherichia coli*, *Stenotrophomonas maltophilia*, *Aeromonas sobria* and *Pseudomonas aeruginosa*.

2.3.1.1. Antimicrobial activity measurement. For the preparation of a functional solution aimed at evaluating the inhibition zones and minimal inhibitory concentrations, all compounds **3** and **3a–c** were dissolved in DMSO. Subsequently, the concentration was diluted to create a solution of 1000 μg mL^{-1}. The both compare the antibacterial efficacy and validate the method, a reference standard of azithromycin at a concentration of 30 mg mL^{-1} was utilized.

2.3.1.2. Evaluating inhibition zones. The antimicrobial effectiveness of all the synthesized compounds (**3** and **3a–c**) was examined against different strains of both Gram-positive and Gram-negative bacteria. To evaluate this, compounds **3** and **3a–c** were utilized in disk diffusion assays on Mueller–Hinton agar medium to measure the extent of the inhibition zones.[34,35] Fresh bacterial cultures prepared in sterile physiological water were employed to inoculate individual sterilized Petri plates following the autoclaving of Mueller–Hinton agar medium for 30 min. Subsequently, the cultures were placed on agar plates with sterile 6 mm filter paper discs soaked in the chemicals under investigation at concentrations of 1000 μg mL^{-1}. Then the cultures were incubated at 37 °C for 24 h to assess the bacterial growth. For the negative control, disks embedded with DMSO were utilized. The inhibition zones formed on the medium were quantified in millimeters (mm).

2.3.1.3. Minimum inhibitory concentration (MIC). Using sterile 96-well plates, the minimum inhibitory concentration (MIC) was determined in Muller Hinton broth through the serial dilution technique. A range of doses, including 1000, 800, 600, 400, 200, 100, 80, 60, 40, 20, and 10 μg mL^{-1}, was employed to investigate the antibacterial efficacy of the produced compounds (**3** and **3a–c**). In 96-well microplates, 50 mL of standard microbe suspension containing 106 colony forming units (cfu mL^{-1}) was introduced. Then, the microplates were placed in an incubator set at 37 °C for a period of 18 to 24 h, following the guidelines outlined by the McFarland turbidity standards. At the end of the incubation period, the plates were inspected to determine whether growth was present or absent. The minimum inhibitory concentration (MIC) was identified as the lowest concentration that visibly prevented bacterial

growth. Each bacterium was subjected to testing with samples **3** and **3a–c** on three separate occasions.

2.3.2. Induction of burn injuries

2.3.2.1. Animal care. The trial and data gathering were executed at the Biology Department of the University of Raparin. For this experimental model, albino Wistar female rats with an average weight of 190 ± 20 g were employed. Each experimental group was comprised of three rats accommodated in separate cages with dimensions of 40 × 25 × 20 cm. The conventional care and circumstances, including continuous light/dark photoperiod lighting conditions, temperature regulation at 24 °C ± 2 °C, and unrestricted access to food and water, were established. The experimental protocol was executed according to the animal experimentation ethics committee guidelines outlined in DIRECTIVE 2010/63/EU.

2.3.2.2. Burn procedure. The rats were acclimated to the laboratory for 7 days prior to the study. Initially, 18 rats ($n = 3$) were weighed and anesthetized with a mixture of 30% chloroform (70 + 10) mg per kg body weight intramuscularly. After all the rats were accurately anesthetized, their hair was removed using electrical clippers. Thermal injury was induced by heating (20 mm width and 30 mm length) a solid stainless steel spatula on a Bunsen burner until the temperature reached between 165–190 °C, which was measured with a thermometer simultaneously. Approximately 6 cm^2 areas on the dorsal proximal region of the animal skin were contacted with the spatula twice side by side for 10 s to produce thickness burn wounds corresponding to the high temperature of the spatulate, where no pressure was applied on the animal skin in the burn induction.[36,37]

2.3.2.3. Preparation of the cream. Three creams containing compounds **3a–c** at a concentration of 1% w/w were formulated. This was achieved by dissolving 0.05 g of each compound in 2 mL of acetone in a crucible. Subsequently, 5 g of pure paraffin wax was incorporated, followed by sonication and heating to liquefy the wax and eliminate the acetone from the mixture. Then, the mixture was cooled to room temperature while stirring, ensuring the formation of a uniform cream. Next the creams were sterilized in an autoclave *via* steam heat at 121 °C (15 lb per in^2) for approximately 15 min. Following sterilization, the creams were cooled with continuous stirring.[38]

2.3.2.4. Healing of burn wounds. The burned rats were randomly allocated into five primary groups, as follows: the experimental groups (**3a**, **3b**, and **3c**), the positive control group (pure paraffin wax), the negative control group (no treatment), and the standard group (treated with Hamazine 1%) ($n = 3$). Treatment commenced 24 h after the infection. The affected area in each wounded rat was swabbed with one application of these creams. Over a 24 h period, the advancement of burn wound closure was observed and recorded for each group.

2.3.3. Acute cytotoxicity

2.3.3.1. Dose preparation. The necessary quantity of the examined compounds (mg kg^{-1}) relative to body weight was dissolved in ethanol. Subsequently, the mixture was gently heated with continuous stirring to facilitate the dissolution of the tested molecules (**3a–c**), as indicated in Table 5.

2.3.3.2. Dose administration. Following the guidelines set forth by OECD/OCDE 425-27, three animals were weighed, and a restricted test amount of 0.5 mg per kg body weight was administered in a single 24 h dose through the parenteral route. This administration was carried out using a 1 cm^3 tuberculin syringe with a 25 g needle for each compound, with pure ethanol injected in the rats serving as the negative and non-injected rats (non-injected ethanol and **3a–c** substances) as positive controls (as outlined in Table 5). After dosing, the animals were meticulously monitored individually during the initial 6 h (at 30 min intervals), at various intervals over the first 24 h, and subsequently on a daily basis for a period of 14 days. Furthermore, comprehensive notations were made regarding behavioral modifications and noticeable transformations in the eyes, skin, and fur of each rat, in contrast to the control group, over the entire experimental period. On the fifteenth day, the rats were compassionately anesthetized using chloroform in a container, and then subjected to macroscopic examination to evaluate their external appearances as well as abdominal and thoracic organs (Fig. S27–S35†).

2.4. Computational studies

2.4.1. Geometry optimization. Within the domain of computational chemistry, quantum mechanical methodologies are widely employed to calculate molecular orbital properties and molecular electrostatic features.[39] The Gaussian 09 software package was employed to conduct geometry optimization and subsequent refinement of all the synthesized analogs.[40] For optimization, the density functional theory (DFT) approach with the 3-21G basis set, incorporating Becke's and Lee, Yang, and Parr's (LYP) (B) functional, was utilized.[41,42] During this optimization process, water was chosen as the solvent environment. Following the optimization, the chemical descriptors were evaluated using Parr and Pearson's interpretation of DFT and Koopman's theorem.[43] This encompassed all the relevant chemical characteristics, as defined by the provided formula.

$$\Delta_\varepsilon = \varepsilon_{LUMO} - \varepsilon_{HOMO}$$

$$\eta = \frac{\varepsilon_{LUMO} - \varepsilon_{HOMO}}{2} \quad (1)$$

$$S = \frac{1}{\eta} \quad (2)$$

$$\mu = \frac{\varepsilon_{LUMO} + \varepsilon_{HOMO}}{2} \quad (3)$$

$$\chi = -\frac{\varepsilon_{LUMO} + \varepsilon_{HOMO}}{2} \quad (4)$$

$$\omega = \frac{\mu^2}{2\eta} \quad (5)$$

2.4.2. PASS cataloging. The PASS online tool (available at **https://www.pharmaexpert.ru/passonline/**, accessed on July 20,

2023) was employed to ascertain the potential biological effects of the synthesized compounds.[44] Initially, the configurations of molecules **3** and **3a–c** were converted into the SMILES format using the SwissADME web-based tool (**https://www.swissadme.ch**, accessed on July 20, 2023). Afterwards, the SMILES notations were entered in the PASS online server for the computation of the biological profile. The PASS results are displayed in the form of Pa (probability for active compounds) and Pi (probability for inactive compounds). The acceptable range for the Pa and Pi scores is between 0.00 and 1.00. Usually, Pa + Pi does not equal 1 due to the inherent variability in predictions. Biological activities are considered promising for potential drug candidates when Pa is greater than Pi.

2.4.3. Pharmacokinetics and drug-likeness prediction analysis. The pkCSM platform was employed to assess a range of properties for all the synthesized compounds. These properties included water solubility (represented as log mol L^{-1}), permeability in the Caco-2 cell assay (log PAPP), capability for skin penetration, likelihood of human intestinal absorption, extent of plasma protein binding, permeability through the blood–brain barrier, volume of distribution, permeability within the central nervous system (CNS), recognition as a renal OCT2 substrate, total clearance, inhibitory impact on CYP450 1A2, CYP450 3A4, CYP450 2C9, and CYP450 2D6 enzymes, inhibition of the Herg1 channel, potential for human hepatotoxicity, AMES test outcomes, skin sensitivity assessment, and LD_{50} values.[45]

2.4.4. Computational molecular docking analysis. In this study, the technique of *in silico* molecular docking was employed to examine the biomolecular interactions of a novel set of azo-amide compounds (**3a–c**). The objective of this study was to contribute to the enhancement and optimization of therapeutic molecules aimed at effectively inhibiting specific disease-causing proteins. The Molecular Operating Environment software (Moe-Dock 2015.10) was employed to perform molecular docking studies on each of the compounds (**3a–c**).[46] By utilizing the build function, the aforementioned compounds were assigned to their respective structures. In addition, the MOE program utilized the default MMFF94x force field to perform energy minimization on these compound configurations, ensuring their readiness for subsequent docking analyses. The three-dimensional structure of the target protein was created using the binding protein information from the Protein Data Bank entry with the identifier 1KZN (accessible at **https://www.rcsb.org/structure/1KZN**). The MOE-Alpha site finder was employed to pinpoint the active site in 1KZN, and subsequently MOE Dock was utilized for docking the ligands. The MOE software also facilitated the determination of the optimal interaction scores between the ligands and the active site. The most favorable ligand-active site interactions were highlighted by selecting the top five conformers of the ligands that demonstrated the highest and most advantageous scores. To validate the docking method, the ligand was re-docked into the active site, yielding binding interactions similar to that observed with a co-crystallized ligand. The root mean square deviation (RMSD) between the re-docked ligand and the co-crystallized ligand was less than two units, affirming the reliability of the docking procedure.

2.4.5. Deformability, *B*-factor, and covariance analysis. Subsequently, an additional molecular dynamics simulation (MDS) of the two complexes was conducted using the iMOD server. The iMOD server employed normal mode analysis to assess the stability of the complexes by analyzing their internal coordinates. Utilizing the iMODS software, deformability, *B*-factor, and covariance calculations were performed to provide insights into the overall stability of the complexes.[47]

2.4.6. Molecular dynamics study. Compounds **3a–c**, which demonstrated the most favorable binding affinity with the target protein (1KZN of *E. coli*), were selected for an in-depth molecular dynamics (MD) simulation investigation utilizing the GROMACS-2021.4 software platform.[48] Comprehensive molecular dynamics (MD) simulations were conducted on the protein–ligand complexes that emerged from the initial binding affinity prediction analysis. These simulations were carried out in parallel with the original crystal structure of the target proteins bound to the co-crystal inhibitor. The protein–ligand complexes underwent an initial cleaning and preparation process utilizing the macromolecule tool in Chimera version 1.17.2.[49] The protein topology files were established employing the Charmm27 force field, incorporating the TIP3P water model. For ligand topology generation, the ligand was initially converted to the LIG.mol2 format using Chimera 1.17.2, and hydrogen atoms were added. Subsequently, the required parameters were calculated using the online generation tool located at **https://www.swissparam.ch/**.[50] The topology and coordinate information for both the protein and ligand were then amalgamated, resulting in the creation of an independent system. The system was solvated by introducing 26 994 water solvent molecules, and to ensure neutrality, counter ions were included. Specifically, Na^+ ions were added to balance the charge in the dodecahedron box. The solvated system underwent an energy minimization process using the steepest descent algorithm, with a total of 5000 steps. This procedure was implemented to rectify any erroneous contacts and steric clashes in the protein–ligand complexes, ensuring structural integrity and stability. The system underwent equilibration at a consistent temperature of 300 K using the *NVT* (number of particles *N*, volume *V*, and temperature *T*) ensemble, with a duration of 100 ps. Subsequently, equilibration using the *NPT* (number of particles *N*, pressure *P*, and temperature *T*) ensemble was conducted for an additional 100 ps. The ultimate molecular dynamics (MD) production run was executed at 1 bar pressure and 300 K for an extensive duration of 500 000 000 integration steps, which is equivalent to a simulation time of 100 ns. The output data generated were plotted using Xmgrace, and then visualized and refined using Origin 2022.

2.4.6.1. Calculation of binding free energy using the molecular mechanics-Poisson Boltzmann surface area (MM-PBSA) method. The determination of the affinity of a compound to a biological macromolecule or target, as well as the assessment of the thermodynamic stability of the protein–ligand complex heavily depend on the binding free energy (ΔG) calculation through the

MM-PBSA approach.[51] This technique provides a quick and accurate prediction of the absolute binding potency of a compound within the active binding site of a target protein, highlighting the significance of the binding free energy as a pivotal factor in both the stability of the compound and its specific effectiveness.[52] Following the completion of the molecular dynamics simulations, the determination of the binding free energies for each protein–ligand complex was carried out using the binding free energy in GROMACS-2021.4 software platform, incorporating the MM-PBSA methodology. Throughout this analysis, the binding free energies were computed for all the generated conformations, resulting in the calculation of the average binding free energy (ΔG) for each unique protein–ligand complex.

3 Result and discussion

3.1. Chemistry

The initial starting material, an azo compound referred to as 2-hydroxy-5-(thiazol-2-yldiazenyl)benzoic acid (**3**), was created through the reaction between a diazonium salt (thiazole-2-diazonium chloride) serving as the electrophilic element and an electron-rich aromatic coupling partner, specifically 2-hydroxybenzoic acid (salicylic acid). This synthesis adhered to an electrophilic aromatic substitution mechanism. The presence of the hydroxyl group (in 2-hydroxybenzoic acid) directed the aryl diazonium ion to the *para* position, unless this position was already occupied. If the *para* position was inaccessible, the ion would instead bind to the *ortho* position.[53] The azo-thiazole bearing thiazole moiety derivatives (**3a–c**) were prepared through a reaction involving aromatic amines (**a–c**) and 2-hydroxy-5-(thiazol-2-yldiazenyl)benzoic acid (**3**) in toluene as the solvent (as illustrated in Scheme 1). The structure of compounds **3** and (**3a–c**) was verified by examining their spectral data and elemental composition. The proposed structures were substantiated by congruent outcomes obtained from diverse spectroscopic and analytical techniques, including ^{1}H NMR, ^{13}C NMR, FT-IR, and HRMS. In the FT-IR spectra of azo compound **3**, an absorption band at 1580.83 cm^{-1} was detected, indicating the presence of the azo (N=N) functional group.[73–75] Furthermore, a noticeable peak emerged at 1655.85 cm^{-1}, suggesting the existence of a carboxylic functional group (C=O). In the FT-IR spectrum of compound **3**, a broad spectral feature was observable at approximately 3232.05 cm^{-1}, which corresponds to the absorption of the O–H group. The ESI† provides the IR spectra of the prepared azo compounds (**3** and (**3a–c**)), as depicted in Fig. S1–S4.† The spectra of compounds **3a–c** reveal distinct bands in the range of 3116.31 to 3232.13 cm^{-1} and 3006.51 to 3090.69 cm^{-1}, which are assigned to the ν(OH) and ν(Ar–H) stretching vibrations, respectively. The peaks observed between 1655.05 and 1668.25 cm^{-1} and 1578.20 and 1578.76 cm^{-1} correspond to the stretching vibrations of the ν(C=O) and ν(N=N) bonds, respectively. In the FT-IR spectra of **3a–c**, discernible bands representing the (C–N) and (C–O) frequencies were identified in the range of 1377.49 to 1380.74 cm^{-1} and 1153.39 to 1155.61 cm^{-1}, respectively. The ESI (Fig. S5–S8†) provides the ^{1}H NMR spectra for **3** and **3a–c**, respectively. These spectra distinctly show signals that are exchangeable with D_2O. Notably, a signal appeared at 12.26 ppm, signifying the phenolic hydroxyl proton, while another notable signal was observed at 12.99 ppm, indicating the presence of the carboxylic proton in compound **3**. Moreover, the synthesized compounds **3a–c** displayed a singular singlet in the range of 11.30–11.96 ppm, which is attributed to the amide protons (C=ONH). Additionally, compound **3** exhibited a strong singlet at δ12.99 ppm, confirming the –OH proton in the carboxylic group. However, in derivatives **3a–c**, this chemical shift disappeared and new peaks resonated at δ10.63–11.52 ppm, corresponding to the protons of the new synthesized amides. In the ^{13}C NMR spectrum, compound **3** exhibited a resonant peak at 172.42 ppm, corresponding to the carbonyl carbon of the carboxylic group. In contrast, this peak shifted to 176.69–176.74 ppm in the molecules of derivatives **3a–c**, confirming the formation of the synthesized amides (**3a–c**) and indicating an increase in their shifting due to the deshielding of the carbonyl carbon. The ESI (Fig. S13–S16†) displays the HRMS spectra of the newly synthesized thiazole-bearing amide moieties (**3a–c**), respectively. In the HR-MS spectra of molecules **3a–c**, distinctive molecular ion peaks were observed, attributed to the $[M–H]^+$ ions at m/z 332.02, 381.04 and 471.01 for **3a**, **3b**, and **3c**, respectively. These values are consistent with their corresponding molecular weights of 331.019, 381.053, and 472.019, respectively. The resulting molecular ion peaks closely correspond to the calculated molecular weights of the prepared azo-bearing amides (**3a–c**).

3.2. UV-vis spectra and electronic properties

The UV-vis spectra of products **3** and **3a–c** were recorded in the range of 200–900 nm in five organic solvents with varying polarities (ethanol, DMSO, DMF, benzene, and toluene) under ambient conditions, as shown in Fig. 1. The UV-vis absorbance patterns of **3** and **3a–c** in polar aprotic solvents (DMSO and DMF) exhibited three distinct bands in the range of 293 to 477 nm (Fig. 2). The spectral peaks observed in the range of 293–302 nm and 389–433 nm are linked to the $\pi \rightarrow \pi^*$ transitions taking place in the aromatic ring structure, indicating a shift towards longer wavelengths (bathochromic shift). The third absorption region, situated between 438 and 477 nm, can be ascribed to the intermolecular charge transfer interactions involving the compound and the solvent[54] (Table 1). This phenomenon arises from the existence of a modest intermolecular hydrogen bonding and an azo-aromatic chromophore in the structure, leading to $n \rightarrow \pi^*$ transitions in the system. The presence of a hydroxyl group in molecule **3** causes a slightly more intense absorption spectrum, displaying a hyperchromic effect compared to similar analogs containing amide groups. This distinction is particularly evident in the case of **3c**. The underlying reason for this phenomenon is the higher electron-donating capability of the core structure of molecule **3** in contrast to its derivatives (**3a–c**). This enhanced electron-donating ability is attributed to the presence of electron-rich hydroxyl groups. Consequently, it results in a more pronounced intermolecular charge transfer (ICT) and electron

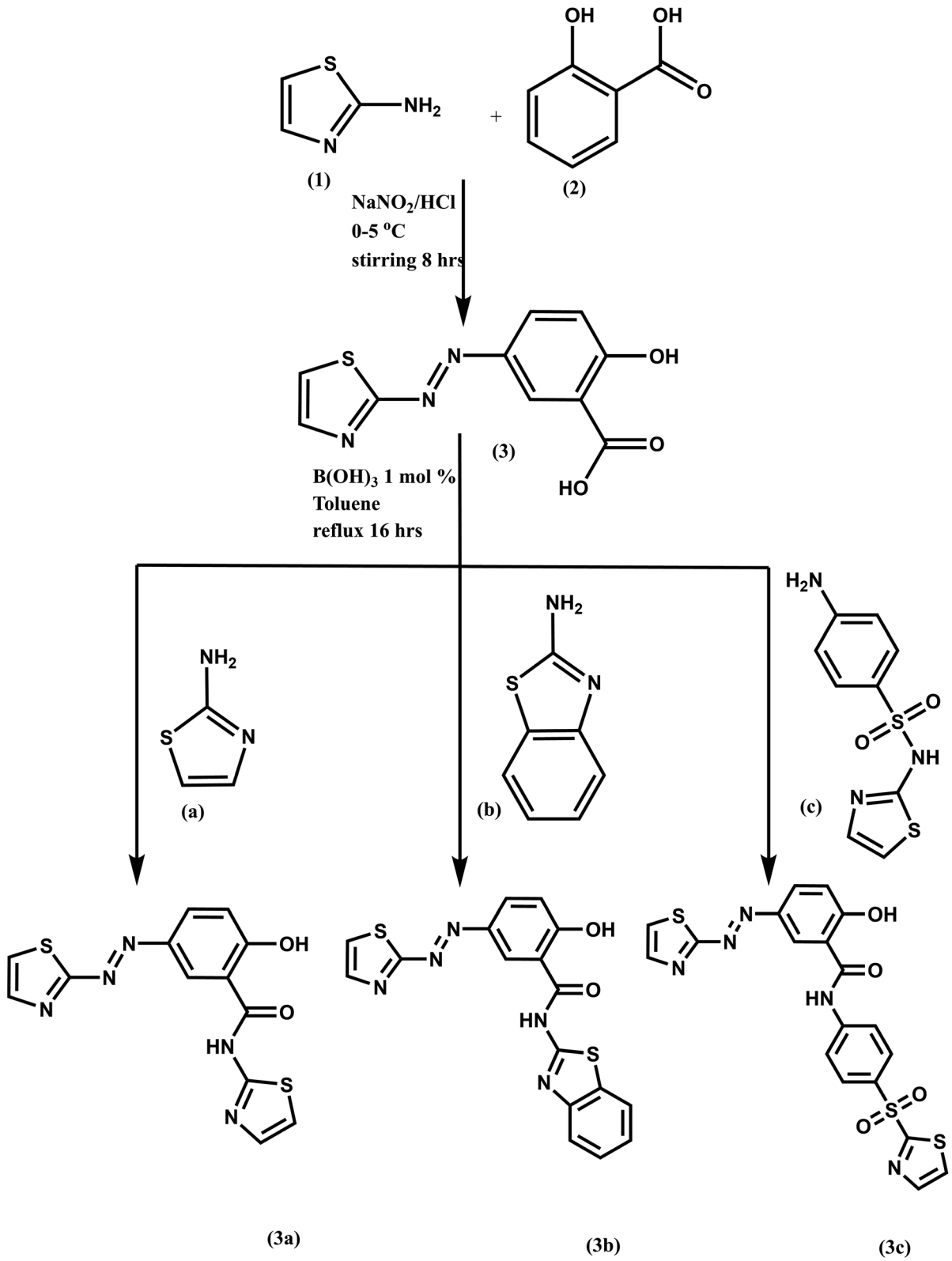

Scheme 1 A schematic of the synthesis of compounds 3a–c.

density effect toward the azo side of the molecule (Fig. 3). In the ethanol, benzene, and toluene solvents, the molecular arrangement (as illustrated in Fig. 1) distinctly exhibits two well-defined spectral bands. The initial band, observable in the wavelength range of 291–311 nm, originates from the $\pi \rightarrow \pi^*$ transitions involving both the aromatic ring and the

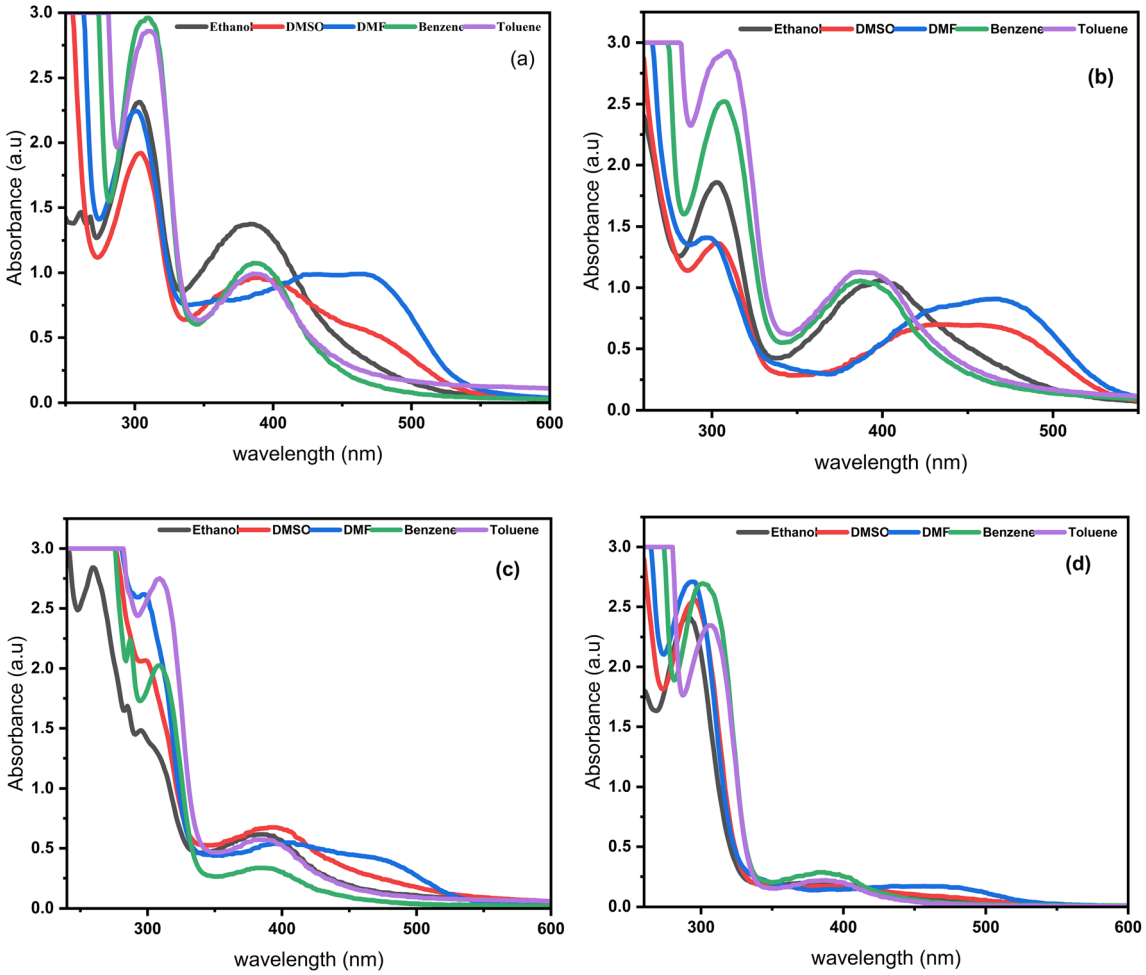

Fig. 1 The UV-vis spectra of the synthesized molecules recorded in different solvents (a) **3**, (b) **3a**, (c) **3b** and (d) **3c**.

azomethine group. Simultaneously, a lower-energy shift (n → π*) becomes noticeable, falling in the spectral range of 384–388 nm. This transition can be attributed to the intricate interplay of electronic effects between the azo-aromatic chromophore and the phenomenon of intramolecular charge transfer. This interplay holds significance across the entirety of

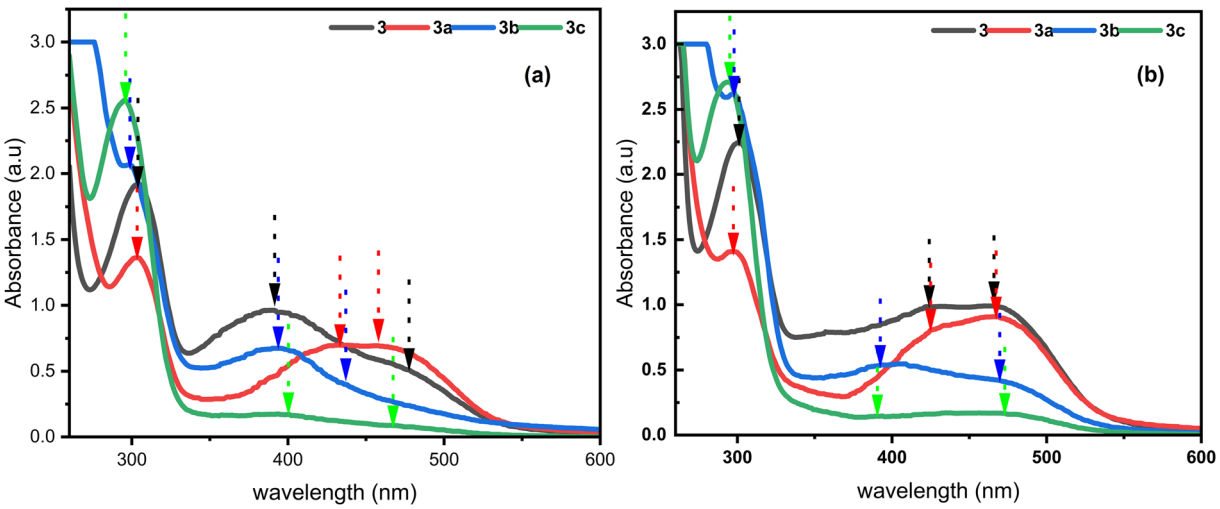

Fig. 2 The UV-vis spectra of compounds **3** and **3a–c** recorded in (a) DMSO and (b) DMF solvents.

Table 1 The influence of alterations in the solvent conditions on the peak absorption wavelength (λ_{max}) of compounds **3** and **3a–c**

		Absorption bands (nm)		
Entry	Solvent	1st (π–π*)	2nd (π–π*, n–π*)	3rd (n–π*)
3	Ethanol	303	384	—
3a		303	401	—
3b		296	388	—
3c		291	394	—
3	DMSO	302	391	477
3a		303	433	459
3b		300	393	438
3c		295	400	468
3	DMF	301	422	468
3a		298	426	467
3b		298	396	470
3c		293	389	473
3	Benzene	310	386	—
3a		307	386	—
3b		309	388	—
3c		301	386	—
3	Toluene	311	388	—
3a		310	384	—
3b		309	386	—
3c		306	387	—

the meticulously crafted dye molecules. The attributes of these absorption bands are influenced by both the solvent employed and the substitutions introduced. In DMSO and DMF solvents, the transitions exhibited a shift towards shorter wavelengths (hypsochromic shift), accompanied by lower absorption intensities compared to benzene and toluene. When considering the n → π* transition, it is observed that hydrogen bonding with the ground states of molecules occurs more readily than with their excited states (Fig. 3). Consequently, there is an elevation in the energy of electronic transitions, resulting in a shift towards lower energy levels for the transitions. In the context of π → π* transitions, interactions involving dipole–dipole interactions with solvent molecules induce a more pronounced decrease in the energy of the excited state in comparison to the ground state. This phenomenon leads to the excited states exhibiting a greater level of polarity than the ground state, as elucidated in ref. 55–58. The modifications in the dipole moment occurring during the excited state or variations in the strength of hydrogen bonding in polar solvents are factors that contribute to the observed redshift, a phenomenon that becomes evident in the synthesized compounds.

3.3. Biological study

3.3.1. Antibacterial activity. *In vitro* bacterial resistance testing was conducted against isolated pathogens, including Gram-positive bacteria such as *Bacillus cereus*, *Staphylococcus aureus* and *Staphylococcus epidermidis*, as well as Gram-negative bacteria such as *Escherichia coli*, *Stenotrophomonas maltophilia*, *Aeromonas sobria*, *Pseudomonas aeruginosa* and *Klebsiella pneumoniae*. Standard established drugs (azithromycin) were employed for comparison.[32] The effectiveness of azo-thiazole 3 and the newly developed thiazole-containing azo-thiazole compounds **3a–c** in preventing microbial growth was assessed through qualitative and quantitative means. A see-through ruler was employed to gauge the width of the transparent zone of inhibition around 6 mm-wide paper discs. Furthermore, the minimum inhibitory concentration (MIC), denoting the smallest concentration of substances that can hinder bacterial growth, was ascertained (refer to Fig. S17–S20†), respectively.

3.3.1.1. Determination of inhibition zones. In addition to synthetic molecules **3** and **3a–c**, it is important to highlight the significant inhibition of growth in the tested bacterial pathogens. As detailed in Table 2, compounds **3** and **3a–c** displayed inhibitory zones, measured in millimeters, ranging from 8 ± 0.11 to 18 ± 0.26 mm against the microbial pathogens. The positive control, azithromycin, displayed values of 7 ± 0.14 and 7 ± 0.32 mm against *Pseudomonas aeruginosa* and *Escherichia coli* pathogens, respectively. In contrast, all the synthesized compounds (**3** and **3a–c**) exhibited enhanced antibacterial efficacy, ranging from 9 ± 0.00 to 10 ± 0.33 mm, against these pathogens. The antimicrobial test results are presented in Table 2 and visually represented in Fig. 4. Among the synthesized compounds, compound **3a** demonstrated the most prominent antibacterial efficacy, manifesting a remarkable measurement of 18 ± 0.26 mm against the tested microorganism, *Staphylococcus epidermidis*. This heightened effectiveness can potentially be attributed to the presence of two thiazole groups in the core structure of compound **3a**. Predominantly, compound **3c** demonstrates enhanced antibacterial effectiveness against *Staphylococcus aureus*, *Staphylococcus epidermidis*, and *Klebsiella pneumoniae*, displaying inhibition zones measuring 16 ± 0.09, 12 ± 0.43, and 12 ± 0.11 mm, respectively. On the contrary, compound **3** displayed considerably diminished antibacterial effectiveness, leading to smaller zones of inhibition against *Bacillus cereus* (10 ± 0.03 mm) and *Stenotrophomonas maltophilia* (8 ± 0.11 mm). Moreover, looking at the bigger picture, the recently created compounds exhibited improved antibacterial potency against both Gram-positive *Staphylococcus epidermidis* and Gram-negative *Escherichia coli*, as well as pathogenic bacteria such as *Pseudomonas aeruginosa*. This antibacterial potential was compared to that of the widely used antibiotic drug azithromycin. Due to the ambiguous mechanism of action of organic compounds against bacteria, numerous researchers have undertaken investigations to explore their antibacterial impacts on microorganisms using diverse binding and interaction mechanisms.[59] Particularly, the observation of bonds being established between pharmaceutical compounds and bacterial cell walls, encompassing hydrogen bonds, has been linked to the initiation of cellular deterioration.[60] Furthermore, an identified element that contributes to the augmentation of antimicrobial effectiveness entails the existence of electron-rich moieties on pharmaceutical compounds. In the context of the synthesized compounds **3a–c**, these functional groups equip them to function as potent antimicrobial agents.[61]

3.3.1.2. Minimum inhibitory concentration (MIC). The antibacterial efficacy of the synthesized compounds, denoted as **3** and **3a–c**, was scrutinized through minimum inhibitory concentration (MIC) analysis. Notably, these compounds

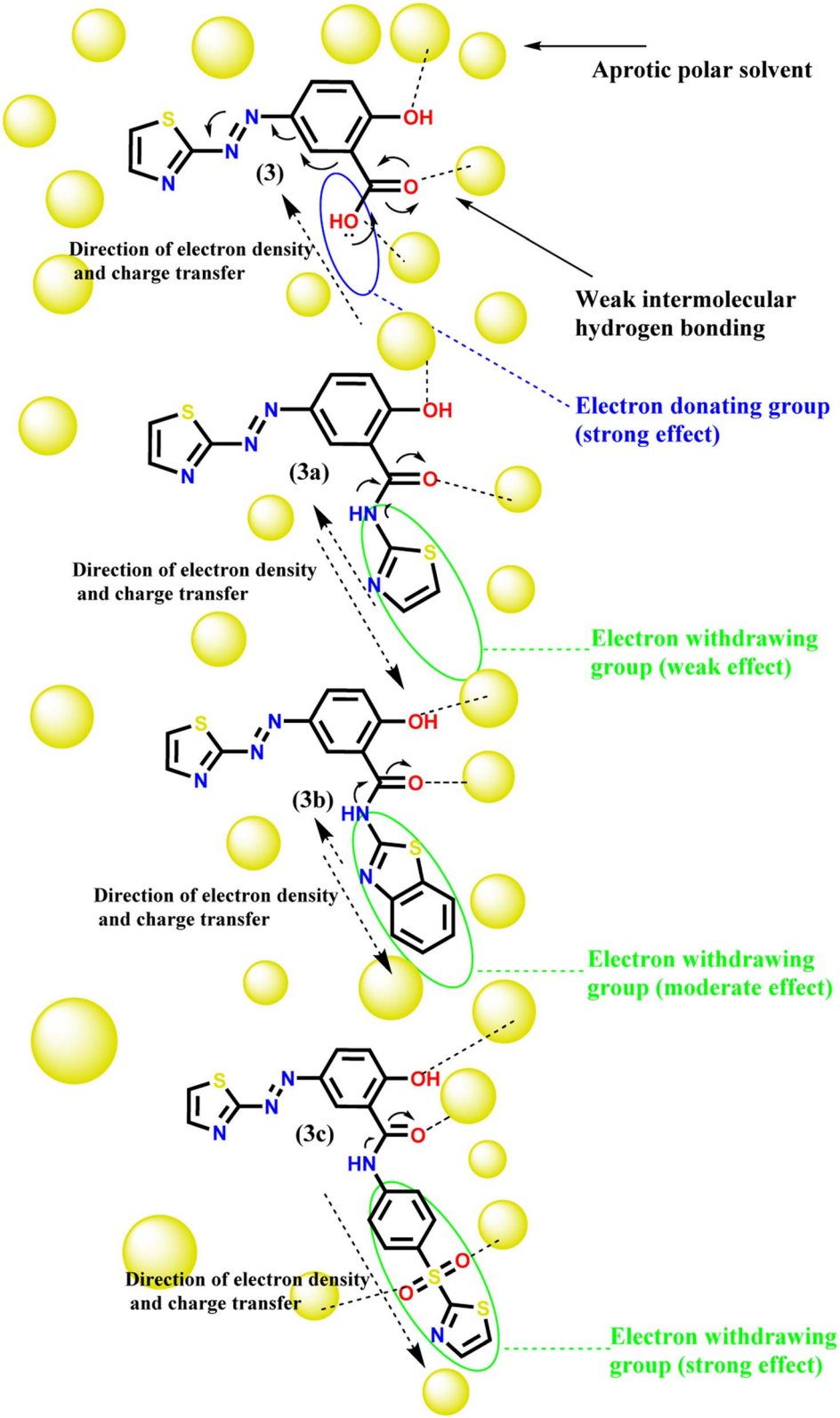

Fig. 3 A schematic diagram of the solvation effect on the n–π* transitions.

displayed pronounced antimicrobial activity against *Staphylococcus aureus* and *Aeromonas sobria*, manifesting the most potent inhibition at remarkably low concentrations, ranging from 10 to 40 μg mL^{-1}. In contrast, their effectiveness against *Bacillus cereus*, *Klebsiella pneumoniae*, and *Pseudomonas aeruginosa* was comparatively modest, necessitating concentrations

Table 2 The antimicrobial efficacy of the synthesized compounds (3 and 3a–c)

	Zone of inhibition (mm)							
	Gram-positive			Gram-negative				
Entry	[a]*B.c*	[b]*S.a*	[c]*S.e*	[d]*K.p*	[e]*E.c*	[f]*S.m*	[g]*A.s*	[h]*P.a*
3	10 ± 0.03	12 ± 0.23	14 ± 0.25	11 ± 0.31	9 ± 0.00	8 ± 0.11	10 ± 0.31	10 ± 0.33
3a	10 ± 0.23	13 ± 0.21	18 ± 0.26	13 ± 0.22	9 ± 0.33	9 ± 0.28	10 ± 0.15	9 ± 0.00
3b	10 ± 0.33	13 ± 0.58	14 ± 0.23	14 ± 0.28	9 ± 0.14	10 ± 0.04	10 ± 0.28	9 ± 0.00
3c	10 ± 0.13	16 ± 0.09	12 ± 0.43	12 ± 0.11	9 ± 0.16	9 ± 0.21	10 ± 0.33	9 ± 0.33
(+ve) azithromycin	11 ± 0.31	15 ± 0.09	11 ± 0.32	20 ± 0.26	7 ± 0.32	10 ± 0.02	18 ± 0.41	7 ± 0.14
(−ve) DMSO	0	0	0	0	0	0	0	0

[a] *Bacillus cereus*. [b] *Staphylococcus aureus*. [c] *Staphylococcus epidermidis*. [d] *Klebsiella pneumoniae*. [e] *Escherichia coli*. [f] *Stenotrophomonas maltophilia*. [g] *Aeromonas sobria*. [h] *Pseudomonas aeruginosa*.

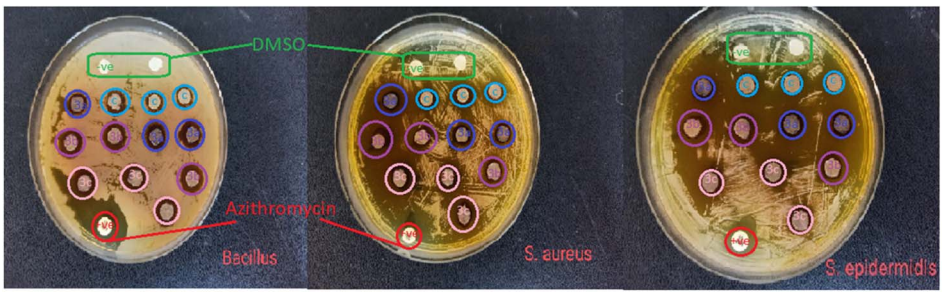

Fig. 4 The antimicrobial effects of compounds 3 and 3a–c were evaluated using the disc diffusion technique at a concentration of 1000 μg mL^{-1}.

within the range of 40 to 200 μg mL^{-1} to elicit discernible antibacterial effects. The MIC technique, conducted across a concentration gradient ranging from 10 to 1000 μg mL^{-1} and documented in Table 3 and Fig. S17–S20,† provided insights into these trends, respectively. Particularly, it was noteworthy that compounds **3b** and **3c** exhibited exceptional antimicrobial potential against *Escherichia coli*, as evidenced by their notably lowest MIC value of 20 μg mL^{-1} compared to the other synthesized compounds. These findings collectively underscore the compound-specific variations in the antibacterial efficacy across diverse bacterial strains, thereby delineating the potential of these synthesized compounds as candidates for further investigation as agents with targeted antibacterial activity.

3.3.2. Burn healing assays. The burn healing assay provides valuable insights into the potential therapeutic effects of different compounds or treatments on burn injuries. In this study, an animal model was employed to assess the potential of these substances for facilitating burn healing in a living system. In the past few decades, *Staphylococcus aureus* has emerged as a prevalent pathogen isolated from burn patients. The heightened pathogenicity of *S. aureus* is attributed to its production of diverse exotoxins, which play a role in the persistence of non-healing wounds and the challenges encountered in achieving successful skin grafting.[62] The active compounds **3a–c**, which exhibited potent antibacterial activity against *S. aureus* in the *in vitro* studies, were further investigated in the form of a cream

Table 3 The minimum inhibitory concentrations of compounds 3 and 3a–c

	MIC (μg mL^{-1})							
	Gram-positive			Gram-negative				
Entry	[a]*B.c*	[b]*S.a*	[c]*S.e*	[d]*K.p*	[e]*E.c*	[f]*S.m*	[g]*A.s*	[h]*P.a*
3	20	10	10	80	60	40	20	80
3a	100	10	80	200	80	60	40	60
3b	80	20	10	80	20	20	10	40
3c	200	10	40	100	20	40	40	100
Positive control (azithromycin)	80	20	80	60	20	40	20	100

[a] *Bacillus cereus*. [b] *Staphylococcus aureus*. [c] *Staphylococcus epidermidis*. [d] *Klebsiella pneumoniae*. [e] *Escherichia coli*. [f] *Stenotrophomonas maltophilia*. [g] *Aeromonas sobria*. [h] *Pseudomonas aeruginosa*.

Table 4 An elaboration on the milligram (mg) quantities employed for each treated group

Compounds	1% cream total weight (g)	Remaining post-treatment (g)	Cream employed for treatment	Day utilized for recovery	Cream per dose per day	Daily mg dosage of each compound
3a	8	3.8	4.2	26	0.161	1.61
3b	8	3.6	4.4	24	0.183	1.83
3c	8	4.1	3.9	27	0.145	1.45
Hamazine	24	12.4	11.6	28	0.414	4.14

(1%). This investigation was conducted in comparison to Hamazine (1%), a standard drug. Rats with burn injuries were subjected to daily treatment with a single dose of approximately 2 mg administered over a 24 h period for the groups undergoing treatment, as outlined in Table 4. The progress of burn healing was monitored for each group, as depicted in Fig. S21–S26.† Specifically, the results pertaining to compound **3a** are illustrated in Fig. 5.

3.3.3. Acute toxicity. Compounds **3a**, **3b**, and **3c** were subjected to initial acute parenteral toxicity testing on rats at concentrations ranging from 0.5 to 50 mg per kg body weight. The objective of this assessment was to establish the concentration at which 50% lethality occurs. Over the course of the study, no occurrences of mortality were noted, and the rats did not display any noteworthy signs of toxicity. The findings in Tables 5 and 6 indicate that the tested compounds were categorized as potentially non-toxic.[63] The rats utilized in this study were humanely euthanized, and their abdominal and thoracic organs were measured for weight. The observed modifications were not attributed to toxicological effects, given that there were no significant variations between the control group and the treated group (Fig. S27–S35†) (Table 5).

3.4. Computational studies

3.4.1. Frontier molecular orbital analysis. Frontier molecular orbitals (FMOs), recognized as one of the most fundamental components in comprehending chemical reactivity and predicting kinetics, are referred to as molecular orbitals[64] (Fig. 6). A substantial energy gap between FMOs signifies robust chemical structural stability and limited reactivity. Typically, the transition of electrons from the stable HOMO to the excited LUMO necessitates additional energy. Table 7 presents

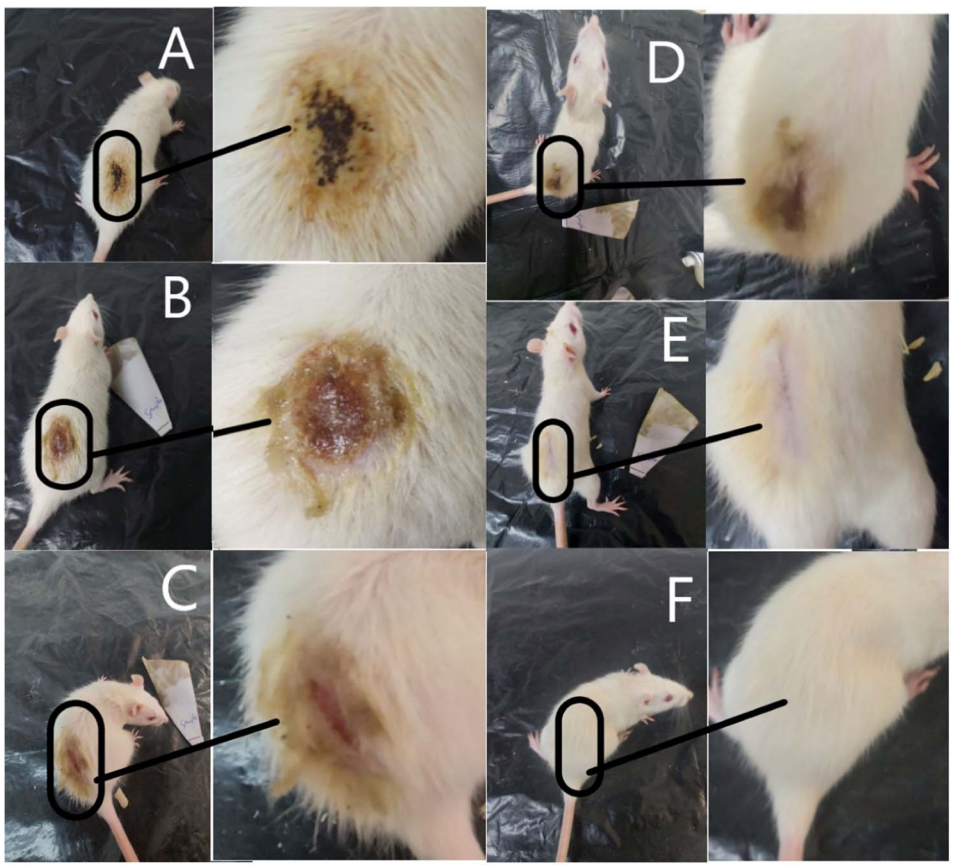

Fig. 5 Variations in the healing advancement of burns on day 1 (A), 3 (B), 12 (C), 14 (D), 17 (E), and 26 (F).

Table 5 The preparation of dosage and administration per rat

Conc. mg kg^{-1}	Ethanol (mL)	Syringe (mL)	No. of doses in 24 h	No. of used rats	Lethality
0.5	5	1	1	3	None
1	5	1	1	3	None
10	5	1	1	3	None
30	5	1	1	3	None
50	5	1	1	3	None

Table 6 Acute toxicity hazard classifications and their corresponding classification system for approximate LD_{50}/LC_{50} (mg kg^{-1}) values established based on OECD 1998b standards, with subsequent updates in OECD 2001

Acute toxicity route	Category 1 (very toxic)	Category 2 (toxic)	Category 3 (harmful)	Category 4 (low toxicity)
Parenteral administration LD_{50}/LC_{50} (mg kg^{-1})	≤0.5	>0.5 and ≤5	>5 and ≤50	>50 and ≤300

a comprehensive overview of various parameters, including the HOMO and LUMO energies, HOMO–LUMO gap (Δ), and other essential chemical descriptors. The combined analysis based on Table 7 and Fig. 6 unequivocally verified that compound **3c** displays a substantial energy divergence of 1.82 eV, whereas compound **3a** exhibits a comparably narrower energy difference of 1.66 eV in comparison to all the other derivatives. Moreover, it is noteworthy that compound **3c** exhibited chemical hardness (η) and softness (S) scores of 0.91 eV and 1.09 eV, respectively, with its softness value standing out as the highest among the derivatives. This observation implies that molecules possessing elevated softness values are more predisposed to electronic alterations, rendering them readily participative in reactions involving electron transfer or electronic rearrangements. Soft molecules, by nature, manifest greater receptiveness and reactivity to external influences. Moreover, compound **3c** with the highest chemical potential (μ) (−7.12 eV) and electronegativity (χ) (7.12 eV) values and lowest electrophilicity (ω) value exhibited good ionization potential or electron affinity and tendency to attract electrons.

3.4.2. Molecular electrostatic potential (MESP) analysis. The concept of MESP enables the identification of binding sites for ligands or proteins and establishes favorable locations for either electrophilic or nucleophilic attack.[65] The MESP is utilized to analyze the dispersion of positive and negative charges across the surface of a molecule, offering insights into its electronic distribution.[66] For all the derivatives **3a–c**, the MESP was computed *via* geometry optimization with the B3LYP/3-21G basis set, as illustrated in Fig. 7. The MESP is of great importance due to its ability to visually represent the molecular size, shapes, and regions of positive, negative, and neutral electrostatic potentials through color gradients. This

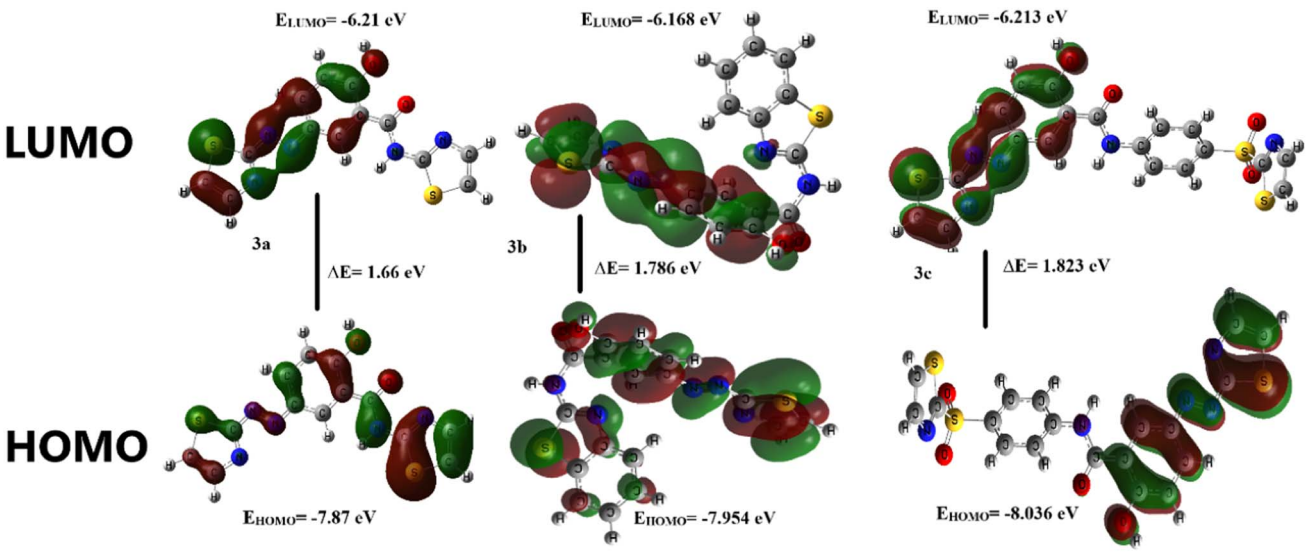

Fig. 6 FMO orbitals and the energy gap between the HOMO and LUMO states in compounds **3a–c**.

Table 7 Molecular descriptors of derivatives 3a–c

Entry	HOMO	LUMO	Gap (Δ_ε)	η	S	μ	χ	ω
3a	−7.870	−6.210	1.66	0.83	1.20	−7.04	7.04	29.85
3b	−7.954	−6.168	1.78	0.89	1.12	−7.06	7.06	27.91
3c	−8.036	−6.213	1.82	0.91	1.09	−7.12	7.12	27.84

characteristic plays a pivotal role in investigating molecular structures and their complex associations with physicochemical characteristics.[67] The computation of MESP was utilized to predict possible reactive locations for nucleophilic and electrophilic reactions in the optimized configurations of derivatives **3a–c**. In this context, the color code employed was red shade indicates regions of highest negativity, signifying favorable positions for electrophilic attacks; blue hue marks zones of highest positivity, conducive to nucleophilic attacks; and green tint corresponds to neutral potential regions.

3.4.3. Analysis of predicted antimicrobial activities using the PASS approach. The web server PASS was employed to assess the antimicrobial potential of all the derivatives (**3a–c**). The PASS outcomes are represented by Pa and Pi values, and their detailed information is presented in Table 8. For derivatives **3a–c**, the Pa values followed the order of 0.286 < Pa < 0.289 for anti-inflammatory activity, 0.234 < Pa < 0.328 for antibacterial activity, and 0.099 < Pa < 0.216 for antiviral activity. These findings indicate that these molecules displayed greater efficacy against bacterial pathogens compared to viral pathogens. The introduction of additional thiazole and aromatic groups led to an enhancement in the anti-inflammatory activity (Pa = 0.289) of **3b** (compared to **3a**, Pa = 0.286). However, the inclusion of the benzene group marginally reduced the antibacterial activity (**3a**, Pa = 0.328 and **3b**, Pa = 0.285). Notably, derivative **3a**, featuring a 4-amino-*N*-(thiazol-2-yl)benzenesulfonamide aromatic group, did not exhibit any anti-inflammatory activity. The antiviral parameters for these derivatives were also predicted.

3.4.4. Analysis of pharmacokinetic profile and drug-likeness. Upon thorough analysis of the physicochemical and ADMET profiling data, it becomes evident that compound **3b** exhibits remarkable characteristics. Notably, it displayed the highest clearance value (0.226) and the most pronounced negative water solubility value (−4.518). Furthermore, compound **3b** demonstrates exceptional attributes, including maximum human intestinal absorption potential (99.813) and significantly enhanced skin permeability (measured at −2.802). Among the molecules examined, **3b** and **3a** exhibited the highest permeation across Caco-2 cells, registering values of 1.01 and 0.763, respectively. Noteworthy plasma protein binding was also observed for these compounds. Compound **3b** displayed the maximum blood–brain barrier permeation with a value of −0.951, while compound **3c** stood out with a distribution volume (V_d) of 0.025. Impressively, **3b** achieved the highest log PS value of −1.925, indicating its substantial central nervous system (CNS) permeability (as detailed in Tables 9 and 10). Evaluating the physicochemical and ADMET data, it becomes evident that most of the molecules adhere to drug-likeness rules. Specifically, compounds **3a** and **3b** met all the defined criteria within the physicochemical and ADMET analyses.

Table 8 Predicted antimicrobial activity of compounds 3a–c

	Anti-inflammatory		Antibacterial		Antiviral	
Entry	Pa	Pi	Pa	Pi	Pa	Pi
3a	0.286	0.174	0.328	0.050	0.216	0.184
3b	0.289	0.171	0.285	0.066	0.099	0.044
3c	—	—	0.234	0.093	0.106	0.038

Table S1† demonstrates that the majority of **3a–c** compounds do not exhibit inhibition of CYP2D6 and CYP2D6 enzymes. Instead, they undergo metabolism by CYP1A2, CYP2C19, and CYP2C9, with the exception of CYP3A4 in the case of compound **3a**. The toxicity results of derivatives **3a–c** are presented in Table S2,† revealing substantial LD_{50} values (ranging from 2.324 to 2.546). This suggests that these analogs may pose lethality concerns only at exceptionally high doses. The negative AMES test results imply the non-mutagenic nature of the amide compound. Furthermore, the data indicates that it is improbable that the tested derivatives will inhibit the hERG channel or induce skin sensitivity.

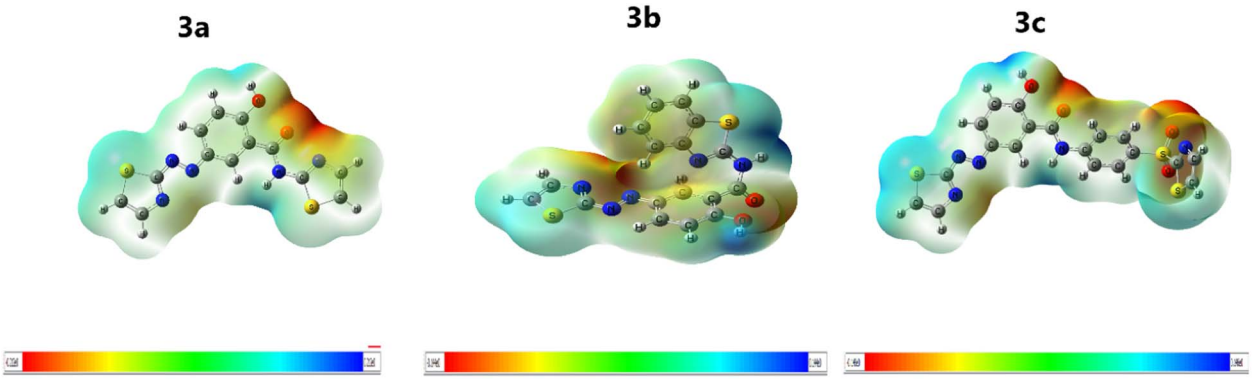

Fig. 7 The molecular electrostatic potential surface of compounds 3a–c.

Table 9 *In silico* prediction of the absorption of derivatives **3a–c**

Entry	Water solubility (log mol L^{-1})	Caco-2 permeability (log PAPP in 10^{-6} cm s^{-1})	Intestinal absorption (% absorbed)	Skin permeability (log K_p)
3a	−4.707	0.763	92.202	−2.93
3b	−4.518	1.01	99.813	−2.802
3c	−3.866	0.358	87.964	−2.743

Table 10 Predicted *in silico* distribution and execration of derivatives **3a–c**

	Distribution				Execration	
Entry	VDss (human) (log L kg^{-1})	Fraction unbound (human) (Fu)	BBB permeability (log BB)	CNS permeability (log PS)	Total clearance (log ml^{-1} min^{-1} kg^{-1})	Renal OCT2 substrate
3a	−0.415	0.178	−1.146	−3.005	0.199	NO
3b	−0.172	0.056	−0.951	−1.925	0.226	NO
3c	0.025	0.079	−1.519	−3.169	−0.002	NO

3.4.5. Studies involving molecular docking. The synthesized compounds **3a–c** were specifically chosen for molecular docking studies against the crystal structure of *E. coli* 24 kDa domain in complex with clorobiocin (1KZN), guided by their antibacterial properties (Fig. 8). It can be asserted that these compounds are snugly accommodated in the binding cavity of 1KZN, as evident from their orientation and binding energy (Table 11). All the compounds subjected to docking exhibited favorable interactions, with a notable emphasis on hydrogen bonding with the protein target. Upon visual inspection, it became apparent that compounds **3a** and **3b**, in particular, can potentially attain stability at the active site through hydrogen bonds involving the sulfur (S) atom of the thiazole moiety. Moreover, compounds **3a** and **3c**, which incorporate five-membered ring functional groups, are anticipated to engage in hydrogen bonding interactions through their pi bonds, thereby enhancing their binding energy. Among the candidates, compound **3a** stood out as the most effective molecule for binding to *E. coli* 1KZN, exhibiting the lowest binding energy at −4.3 kcal mol^{-1}. Two hydrogen bonds are established between the 5-ring of one thiazole group and the sulfur atom of another thiazole group, interacting with the receptor amino acids GLU42 and MET25, respectively. In addition, compound **3c** exhibited a distinctive hydrogen bond interaction with GLY117 (3.16 Å) and displayed the highest binding energy (−0.7 kcal mol^{-1}). The docking studies accurately anticipated the occupancy of the 1KZN binding site by these novel compounds (**3a–c**), thereby suggesting their potential as antibacterial agents.

3.4.6. Deformability, *B*-factor, and covariance computations. The deformability of a ligand–protein complex (1KZN–**3a–c**) refers to the ability of the complex to undergo structural changes or deformations while maintaining its binding affinity and specificity.[68] This deformability can be essential for various biological processes, including ligand recognition, binding, and catalysis.[69] Understanding the deformability of ligand–protein complexes is crucial in drug discovery, molecular modeling, and the design of therapeutic agents (Fig. 9(a)). The obtained trajectories of compound **3a** with protein 1KZN in the complex system reveal a promising and stable binding interaction. The binding of **3a** to the target bacterial pathogen protein appears to be consistent and sustained over time, suggesting a strong and potentially biologically relevant interaction. Furthermore, the analysis of the hinge distortions indicates minimal deformation deviations ranging from approximately 0.18 to 0.85 Å. *B*-Factor investigations of a ligand–protein complex involve studying the temperature or thermal motion of atoms in the complex using *B*-factors (also known as Debye–Waller factors).[70] *B*-Factors provide information about the flexibility and vibrational motion of atoms in a crystal structure or molecular simulation.[71] Analyzing *B*-factors in a ligand–protein complex can offer insights into various aspects of the behavior and interactions of the complex (Fig. 9(b)). The *B*-factor investigations in this study revealed that there is minimal atomic fluctuation within a very narrow range, specifically between approximately 0.15 to 0.8 Å. This limited fluctuation range suggests that the atoms in the system exhibit relatively stable and constrained behavior. Additionally, the use of normal mode analysis further confirms these findings by indicating minimal fluctuations. The Eigen score and variance in normal mode analysis represent the extent of atomic displacement along a given normal mode.[72] A lower Eigen score means that there is less variance or fluctuation along that mode. Specifically, the complex is more stable and rigid along that specific vibrational direction (Fig. 9(c)). The Eigen score of this complex system, which was computed to be 3.493087×10^{-3}, indicates the degree of variance or flexibility present in the normal mode analysis. This score is interpreted as a measure of the compactness of the interacting complex. Specifically, a lower Eigen score suggests a higher degree of compactness and rigidity in the complex. Covariance matrix analysis of ligand–protein complexes is a valuable approach to understand the correlated motions, interactions, and conformational changes that occur upon ligand binding.[73] It can provide mechanistic insights and guide drug design efforts by

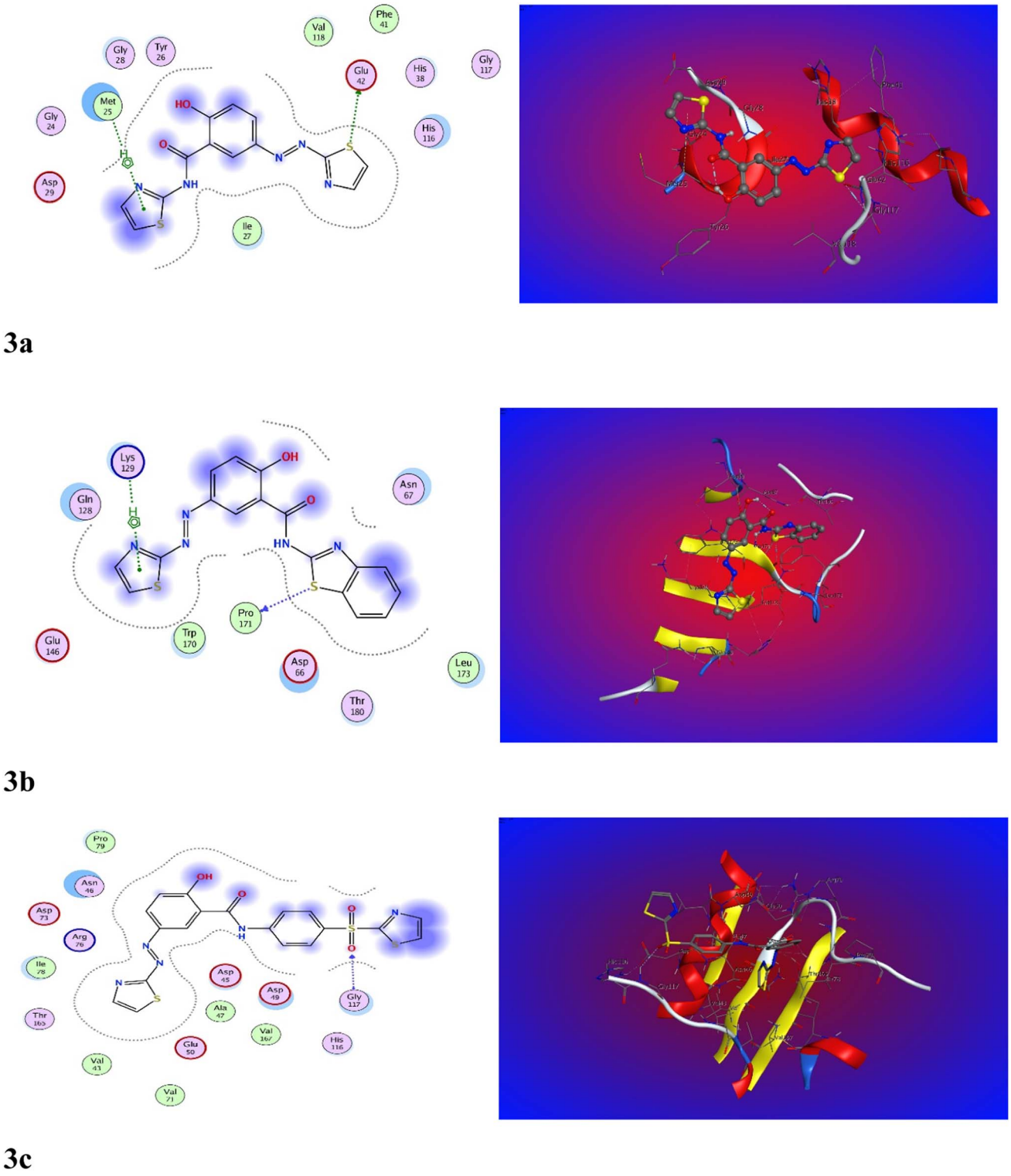

Fig. 8 Explored binding modes in the active site of 1KZN and hydrogen bonds with antibacterial compounds (**3a–c**). Shown in 2D (left) and 3D (right).

revealing functionally relevant dynamics within the complex (Fig. 9(d)). The covariance values illustrate the patterns of coupling between pairs of residues, with the colors red, blue, and white denoting the correlated, anti-correlated, and uncorrelated motions, respectively.[47] Complex **3a** shows a strong correlation with a few instances of anticorrelation, primarily observed.

3.4.7. Molecular dynamics simulations (MDS). The MDS was conducted to gain insights into the flexibility exhibited during various simulation periods. The root mean square

Table 11 Docking studies of different synthesized substances (3a–c) with demonstrated antibacterial activity yielded noteworthy outcomes

Compound	Binding energy (kcal mol^{-1})	Ligand	Receptor	Interaction	Distance (Å)
3a	−4.3	S 31	GLU 42	H-donor	3.37
	−0.8	5-Ring	MET 25	pi-H	4.48
3b	−1.8	S 24	PRO 171	H-donor	3.42
	−1.5	5-Ring	LYS 129	pi-H	3.79
3c	−0.7	O13 19	GLY 117	H-acceptor	3.16

deviations (RMSD) of the C-alpha atoms were employed for analyzing the complexes, aiming to elucidate their structural rigidity (depicted in Fig. 10). The analysis revealed an initial upward trend in flexibility for complexes **3a**, **3b**, and **3c**. However, post 4 ns, the complexes reached a stabilized state and maintained this equilibrium throughout the simulation duration. For all the complexes, the average RMSD remained below 2.17 Å. The minor fluctuations in RMSD indicated the presence of stable conformations in the complexes (as illustrated in Fig. 10(a)). The protein–ligand complex root mean

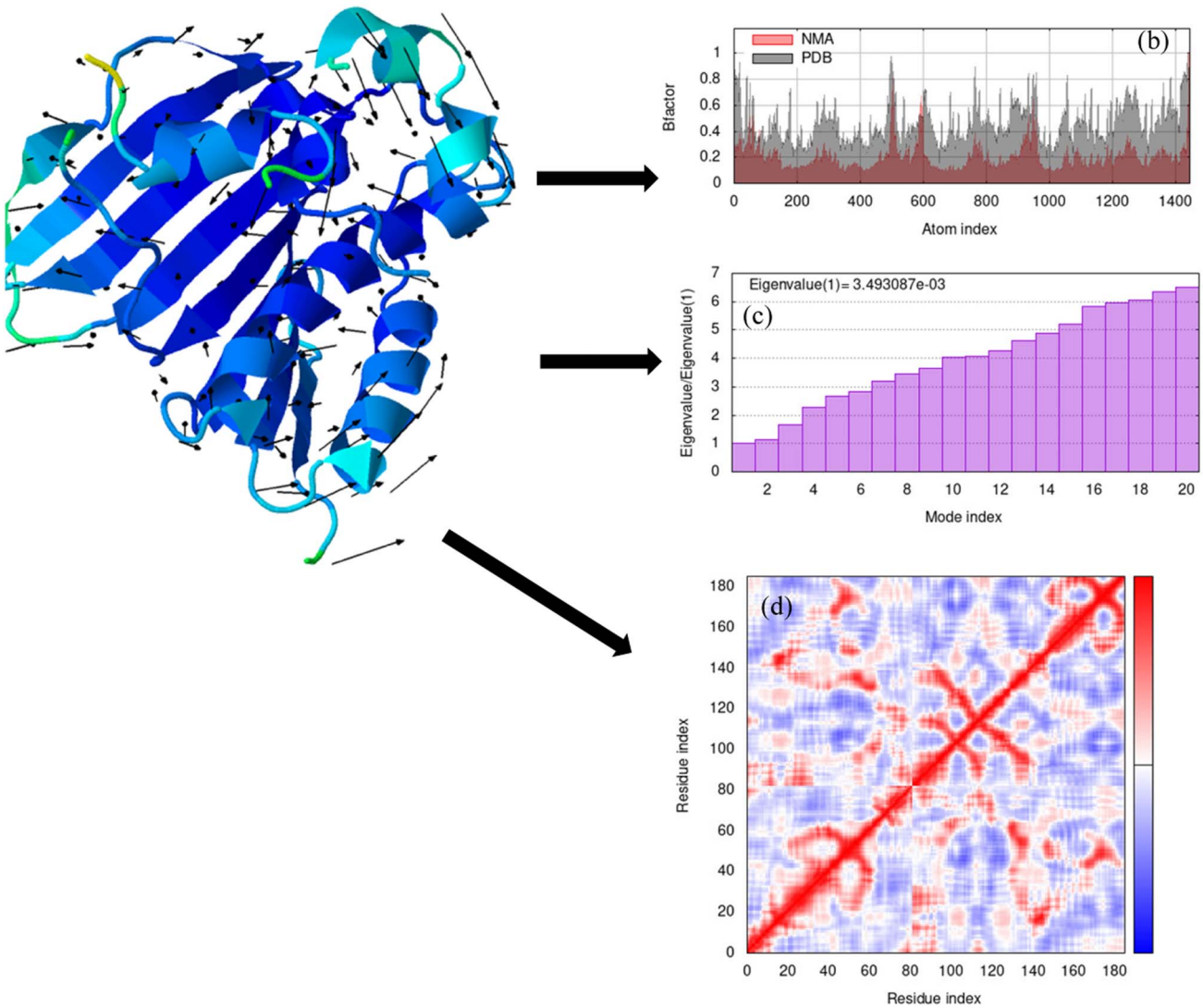

Fig. 9 The globular structure of 1KZN after binding with **3a**: (a) deformability, (b) the *B*-factor, (c) the Eigen score, and (d) the covariance matrix.

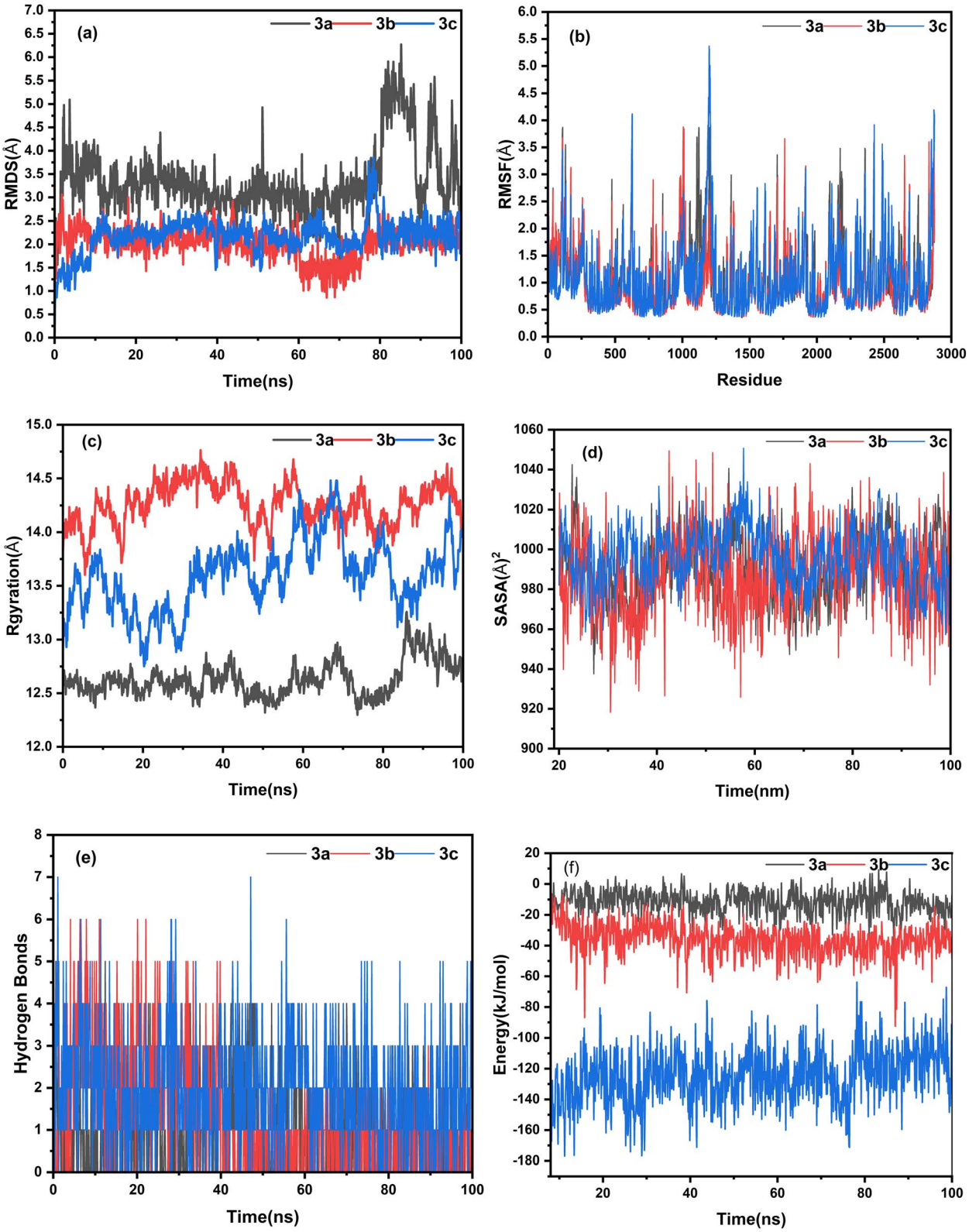

Fig. 10 MD simulation trajectories over 100 ns: (a) the C-alpha atom RMSD, (b) C-alpha atom RMSF, (c) complex gyration radius, (d) solvent accessible surface area of the docked complex indicating the protein area change, (e) complex hydrogen bonds, and (f) binding energy.

square fluctuation (RMSF) was graphed using a 100 ns molecular dynamics (MD) trajectory to assess the typical fluctuation and flexibility of each amino acid individually (Fig. 10). The RMSF plot illustrates that fluctuations in the amino acid residues occur in the protein while in the ligand-bound state, spanning various time intervals. The outcomes indicate that the

interaction between the ligand and the protein results in a closer alignment of the protein chains, leading to a decrease in the distance between them, as demonstrated in Fig. 10(b). The concept of radius of gyration (R_g) is a fundamental metric in the field of structural biology and biophysics, often employed to assess the spatial distribution of mass within a macromolecule or complex. R_g quantifies the compactness or spatial extent of a molecular structure, providing insights into its conformational dynamics and flexibility.[74] The relationship between R_g and molecular flexibility is well-established. A lower R_g signifies that the mass of the molecule is closely distributed around its center, often implying a more constrained and less flexible structure. Conversely, a higher R_g indicates a broader spatial distribution of mass, and by extension a higher potential for conformational changes and flexibility.[75] The observation that complex **3c** has a lower R_g value compared to complex **3b** suggests that **3c** is relatively more compact and structurally constrained, as shown in Fig. 10(c). This implies the specific conformation that complex **3c** tends to adopt, possibly due to tighter interactions or constraints within the complex. Alternatively, the finding that complex **3a** exhibits a higher R_g value compared to complex **4b** indicates that **3a** displays a greater degree of flexibility or conformational variability. This can be due to the weaker interactions, larger structural fluctuations, or potential for different binding modes. Furthermore, the characterization of molecular interactions extends to the solvent accessible surface area (SASA), a critical parameter in structural analysis within the realm of biophysical investigations.[76] The SASA metric serves to illuminate alterations in the accessible surface region, where an augmented SASA value corresponds to an expanded surface area, while a diminished SASA value indicates constrained or truncated complexes.[77] The temporal evolution of the average SASA over the 100 ns trajectory imparts noteworthy insights. Specifically, the SASA analysis revealed that complex **3b** exhibits the lowest SASA trend, quantified at 986.4 Å^2 (Fig. 10(d)). This observation is consistent with the interpretation that complex **3b** adopts more stable conformations in comparison to its counterparts, namely, compounds **3a** and **3c**, which exhibited larger average SASA values of 991.24 Å^2 and 995.97 Å^2, respectively. The intricate hydrogen bond network significantly contributes to establishing the stability of the studied complexes.[78] In the examined complexes **3a**, **3b**, and **3c**, the hydrogen bond pattern was scrutinized, revealing a range from zero to a maximum of five, six, and seven hydrogen bonds, respectively. Computation of their average values yielded 1.038, 1.32, and 1.93 hydrogen bonds, respectively (Fig. 10(e)). The average hydrogen bond count provides an insightful gauge of the frequency and robustness of these vital interactions. Remarkably, complex **3c** exhibited a notably higher average hydrogen bond count (1.93) in comparison to complex **3a** (1.038). This disparity implies that compound **3c** forms a more intricate network of hydrogen bonds with the 1KZN protein. This heightened propensity for hydrogen bonding suggests a heightened level of interaction strength and extent between compound **3c** and the protein.

3.4.7.1. Evaluation of MM-PBSA binding free energy. The application of the MM-PBSA method in evaluating the binding free energy provides valuable information about the potential interaction of a ligand with a receptor and the resulting thermodynamic stability of the formed complex. The stability of the protein–ligand complex formed is particularly crucial in establishing the desired effectiveness of the compound. Hence, we carried out computations of binding free energy for all the conformational states obtained from the 100 ns MD simulations. This process led to the determination of the overall binding free energy. Our analysis revealed that the average binding free energy of complex **3b** is −36.07 kcal mol^{-1}, indicating a more robust interaction compared to complex **3a**, which had a binding free energy of −11.46 kcal mol^{-1}. Notably, the binding free energy of complex **3c** was the lowest at −124.78 kcal mol^{-1} (as depicted in Fig. 10(f)). This discovery is supported by the MIC experimental data for **3c**, where a minimal concentration of 20 μg mL^{-1} was necessary to hinder the growth of *E. coli* colonies. This result highlights the potent inhibitory capability of complex **3c**, which is attributed to its notably low binding free energy.

4 Conclusion

In this study, a novel series of azo-thiazole derivatives (**3a–c**) was synthesized and extensively characterized using various spectroscopic techniques. These compounds were evaluated for their antibacterial and anti-inflammatory properties, and an *in silico* analysis was conducted. Compounds **3a** and **3c** demonstrated significant antibacterial potency against *Staphylococcus aureus*, outperforming azithromycin. Compound **3b** showed remarkable potential in promoting burn wound healing and exhibited strong inhibitory activity against bacterial pathogens. Molecular docking studies confirmed their strong binding affinity to a relevant protein, and their electrochemical characteristics were assessed using DFT calculations. These results highlight that compounds **3a–c** are promising candidates as new active agents in antibacterial and anti-inflammatory applications.

Ethical statement

This work was approved by the Ethical Review Board of the Research Center with the access number (7-29-4964 in 2022). We ensured that all procedures performed in studies involving human participants were in accordance with the ethical standards of the institutional and/or national research committee and with the 1964 Helsinki Declaration and its later amendments or comparable ethical standards.

Data availability

Data will be made available on request.

Author contributions

The manuscript was written through contributions of all authors. All authors have given approval to the final version of the manuscript.

Conflicts of interest

The authors affirm that there are no recognized financial conflicts of interest or personal affiliations that might have seemed to affect the findings reported in this paper.

Acknowledgements

We extend our gratitude to the research center at the University of Raparin for furnishing us with facilities and necessary resources for conducting our research.

References

1 Z. Zheng, *et al.*, Design and synthesis optimization of novel diimide indoles derivatives for ameliorating acute lung injury through modulation of NF-κB signaling pathway, *Bioorg. Chem.*, 2023, **136**, 106557.
2 S. Qiang, *et al.*, Synthesis and Biological Evaluation of Novel FtsZ-targeted 3-arylalkoxy-2, 6-difluorobenzamides as Potential Antimicrobial Agents, *Chem. Biol. Drug Des.*, 2016, **87**(2), 257–264.
3 S. A. Hassan, *et al.*, Design and synthesis of oxazepine derivatives from sulfonamide Schiff bases as antimicrobial and antioxidant agents with low cytotoxicity and hemolytic prospective, *J. Mol. Struct.*, 2023, **1292**, 136121.
4 S. A. Hassan, *et al.*, In vitro and in vivo evaluation of the antimicrobial, antioxidant, cytotoxic, hemolytic activities and in silico POM/DFT/DNA-binding and pharmacokinetic analyses of new sulfonamide bearing thiazolidin-4-ones, *J. Biomol. Struct. Dyn.*, 2023, 1–17.
5 H. Q. Hamad, S. G. Taher and D. M. Aziz, Synthesis and Molecular Docking Studies of New Series of Bis-Schiff Bases Thiadiazoles Derived From Disulfides and Thioethers with Potent Antibacterial Properties, *Science Journal of University of Zakho*, 2022, **10**(3), 130–139.
6 S. A. Hassan and D. M. Aziz, An efficient One-pot three-component synthesis, Molecular docking, ADME and DFT predictions of new series Thiazolidin-4-one derivatives bearing a Sulfonamide moiety as potential Antimicrobial and Antioxidant agents, *Egypt. J. Chem.*, 2022, **65**(8), 133–146.
7 S. A. Hassan and D. M. Aziz, Synthesis of new series bis-3-chloro-β-lactam derivatives from symmetrical bis-Schiff bases as effective antimicrobial agents with molecular docking studies, *Science Journal of University of Zakho*, 2021, **9**(3), 128–137.
8 S. A. Hassan and D. M. Aziz, Synthesis, in vitro Antimicrobial assay and Molecular Docking Studies of some new Symmetrical Bis-Schiff Bases and their 2-Azetidinones, *Zanco Journal of Pure and Applied Sciences*, 2021, **33**(2), 128–137.
9 D. M. Aziz and H. J. Azeez, Synthesis of new ß-lactam-N-(thiazol-2-yl) benzene sulfonamide hybrids: Their in vitro antimicrobial and in silico molecular docking studies, *J. Mol. Struct.*, 2020, **1222**, 128904.
10 M. F. El Shehry, *et al.*, Quinoline derivatives bearing pyrazole moiety: Synthesis and biological evaluation as possible antibacterial and antifungal agents, *Eur. J. Med. Chem.*, 2018, **143**, 1463–1473.
11 M. F. El Shehry, *et al.*, Design, synthesis and biological evaluation of quinoxaline N-propionic and O-propionic hydrazide derivatives as antibacterial and antifungal agents, *Med. Chem. Res.*, 2018, **27**, 2287–2296.
12 M. A. M. S. El-Sharief, S. Y. Abbas, K. A. M. El-Bayouki and E. W. El-Gammal, *Eur. J. Med. Chem.*, 2013, **67**, 263–268.
13 N. Siddiqui, *et al.*, Thiazoles: a valuable insight into the recent advances and biological activities, *Int. J. Pharm. Sci. Drug Res.*, 2009, **1**(3), 136–143.
14 M. Bagheri, *et al.*, Synthesis and Antihypertensive Activity of 1-(2-Thiazolyl)-3, 5-disubstituted-2-Pyrazolines, *Arch. Pharm.*, 2004, **337**(1), 25–34.
15 P. K. Deb, *et al.*, Synthesis, anti-inflammatory evaluation, and docking studies of some new thiazole derivatives, *Med. Chem. Res.*, 2014, **23**, 2780–2792.
16 J. C. Jaen, *et al.*, 4-(1, 2, 5, 6-Tetrahydro-1-alkyl-3-pyridinyl)-2-thiazolamines: a novel class of compounds with central dopamine agonist properties, *J. Med. Chem.*, 1990, **33**(1), 311–317.
17 A. Biernasiuk, *et al.*, Synthesis, antimicrobial activity, and determination of the lipophilicity of ((cyclohex-3-enylmethylene) hydrazinyl) thiazole derivatives, *Med. Chem. Res.*, 2019, **28**, 2023–2036.
18 A. Rauf, *et al.*, Synthesis, anti-HIV activity, molecular modeling study and QSAR of new designed 2-(2-arylidenehydrazinyl)-4-arylthiazoles, *J. Mol. Struct.*, 2019, **1198**, 126866.
19 A. Badorc, *et al.*, New orally active non-peptide fibrinogen receptor (GpIIb-IIIa) antagonists: identification of ethyl 3-[N-[4-[4-[amino [(ethoxycarbonyl) imino] methyl] phenyl]-1, 3-thiazol-2-yl]-N-[1-[(ethoxycarbonyl) methyl] piperid-4-yl] amino] propionate (SR 121787) as a potent and long-acting antithrombotic agent, *J. Med. Chem.*, 1997, **40**(21), 3393–3401.
20 J. Rudolph, *et al.*, seco-Cyclothialidines: new concise synthesis, inhibitory activity toward bacterial and human DNA topoisomerases, and antibacterial properties, *J. Med. Chem.*, 2001, **44**(4), 619–626.
21 L. J. Lombardo, *et al.*, Discovery of N-(2-chloro-6-methyl-phenyl)-2-(6-(4-(2-hydroxyethyl)-piperazin-1-yl)-2-methylpyrimidin-4-ylamino) thiazole-5-carboxamide (BMS-354825), a dual Src/Abl kinase inhibitor with potent antitumor activity in preclinical assays, *J. Med. Chem.*, 2004, **47**(27), 6658–6661.
22 S. Dhillon, Dabrafenib plus Trametinib: A review in advanced melanoma with a BRAF V600 mutation, *Targeted Oncol.*, 2016, **11**, 417–428.
23 D. M. Aziz, S. A. Hassan and O. Q. Hamad, Azo-azomethine complex activity and sensor potential toward Ca (II) ion in life samples: The spectroscopic and morphological studies, *J. Mol. Struct.*, 2023, **1293**, 136204.
24 S. Benkhaya, S. M'rabet and A. El Harfi, Classifications, properties, recent synthesis and applications of azo dyes, *Heliyon*, 2020, **6**(1), 1–26.

25 B. Ravi, *et al.*, Synthesis, characterization and pharmacological evaluation of 2-aminothiazole incorporated azo dyes, *J. Mol. Struct.*, 2020, **1204**, 127493.
26 O. Nagaraja, *et al.*, Synthesis, characterization and biological investigations of potentially bioactive heterocyclic compounds containing 4-hydroxy coumarin, *Heliyon*, 2020, **6**(6), 32–45.
27 Y. Mi, *et al.*, Modification of carboxymethyl inulin with heterocyclic compounds: Synthesis, characterization, antioxidant and antifungal activities, *Int. J. Biol. Macromol.*, 2021, **181**, 572–581.
28 K. Singh, *et al.*, Insights into the structure activity relationship of nitrogen-containing heterocyclics for the development of antidepressant compounds: An updated review, *J. Mol. Struct.*, 2021, **1237**, 130369.
29 C. Viegas-Junior, *et al.*, Molecular hybridization: a useful tool in the design of new drug prototypes, *Curr. Med. Chem.*, 2007, **14**(17), 1829–1852.
30 V. Ivasiv, *et al.*, Molecular hybridization as a tool for designing multitarget drug candidates for complex diseases, *Curr. Top. Med. Chem.*, 2019, **19**(19), 1694–1711.
31 X.-D. Wang, *et al.*, Novel 3-arylfuran-2 (5H)-one-fluoroquinolone hybrid: design, synthesis and evaluation as antibacterial agent, *Bioorg. Med. Chem.*, 2014, **22**(14), 3620–3628.
32 D. muhammed Aziz, *et al.*, New azo-azomethine derivatives: Synthesis, characterization, computational, solvatochromic UV–Vis absorption and antibacterial studies, *J. Mol. Struct.*, 2023, **1284**, 135451.
33 T. Pingwah, Boric acid catalyzed amide formation from carboxyl acids and amines: Nbenzyl-4-phenylbutiramide, *Org. Synth.*, 2005, **81**, 262–267.
34 R. Skov, *et al.*, Phenotypic detection of methicillin resistance in Staphylococcus aureus by disk diffusion testing and Etest on Mueller-Hinton agar, *J. Clin. Microbiol.*, 2006, **44**(12), 4395–4399.
35 R. J. Wallace Jr, J. Dalovisio and G. Pankey, Disk diffusion testing of susceptibility of Mycobacterium fortuitum and Mycobacterium chelonei to antibacterial agents, *Antimicrob. Agents Chemother.*, 1979, **16**(5), 611–614.
36 C. Gaines, *et al.*, Development of a porcine deep partial thickness burn model, *Burns*, 2013, **39**(2), 311–319.
37 D. d. S. Tavares Pereira, *et al.*, Development of animal model for studying deep second-degree thermal burns, *BioMed Res. Int.*, 2012, **2012**, 841–848.
38 M. K. Samad and F. E. Hawaiz, Synthesis, characterization, antioxidant power and acute toxicity of some new azo-benzamide and azo-imidazolone derivatives with in vivo and in vitro antimicrobial evaluation, *Bioorg. Chem.*, 2019, **85**, 431–444.
39 S. Kumaresan, *et al.*, GC-MS analysis and pass-assisted prediction of biological activity spectra of extract of Phomopsis sp. isolated from Andrographis paniculata, *World J. Pharm. Res.*, 2015, **4**(1), 1035–1053.
40 T. Shamsuddin, *et al.*, Uridine derivatives: Antifungal, PASS outcomes, ADME/T, drug-likeliness, molecular docking and binding energy calculations, *Medicine Science*, 2021, **10**, 1373–1386.
41 B. Tüzün and C. Kaya, Investigation of DNA–RNA molecules for the efficiency and activity of corrosion inhibition by DFT and molecular docking, *Journal of Bio- and Tribo-Corrosion*, 2018, **4**, 1–11.
42 A. D. Becke, Density-functional exchange-energy approximation with correct asymptotic behavior, *Phys. Rev. A: At., Mol., Opt. Phys.*, 1988, **38**(6), 3098.
43 C. Lee, W. Yang and R. G. Parr, Development of the Colle-Salvetti correlation-energy formula into a functional of the electron density, *Phys. Rev. B: Condens. Matter Mater. Phys.*, 1988, **37**(2), 785.
44 N. Cohen and S. Benson, Estimation of heats of formation of organic compounds by additivity methods, *Chem. Rev.*, 1993, **93**(7), 2419–2438.
45 D. E. Pires, T. L. Blundell and D. B. Ascher, pkCSM: predicting small-molecule pharmacokinetic and toxicity properties using graph-based signatures, *J. Med. Chem.*, 2015, **58**(9), 4066–4072.
46 S. M. Rangwala, *et al.*, A long-acting PYY3–36 analog mediates robust anorectic efficacy with minimal emesis in nonhuman primates, *Cell Metab.*, 2019, **29**(4), 837–843.e5.
47 J. R. López-Blanco, *et al.*, iMODS: internal coordinates normal mode analysis server, *Nucleic Acids Res.*, 2014, **42**(W1), W271–W276.
48 T. Santos, *et al.*, Stabilization of a DNA aptamer by ligand binding, *Biochimie*, 2022, **200**, 8–18.
49 C. Pouchon, *et al.*, ORTHOSKIM: In silico sequence capture from genomic and transcriptomic libraries for phylogenomic and barcoding applications, *Mol. Ecol. Resour.*, 2022, **22**(5), 2018–2037.
50 J. L. Knight, J. D. Yesselman and C. L. Brooks III, Assessing the quality of absolute hydration free energies among CHARMM-compatible ligand parameterization schemes, *J. Comput. Chem.*, 2013, **34**(11), 893–903.
51 S. Genheden and U. Ryde, The MM/PBSA and MM/GBSA methods to estimate ligand-binding affinities, *Expert Opin. Drug Discovery*, 2015, **10**(5), 449–461.
52 S. Zhong, *et al.*, Improving the performance of the MM/PBSA and MM/GBSA methods in recognizing the native structure of the Bcl-2 family using the interaction entropy method, *Phys. Chem. Chem. Phys.*, 2020, **22**(7), 4240–4251.
53 S. Kucharski, *et al.*, Trans-cis isomerisation of azobenzene amphiphiles containing a sulfonyl group, *New J. Chem.*, 1999, **23**(7), 765–771.
54 S. Roquet, *et al.*, Triphenylamine– thienylenevinylene hybrid systems with internal charge transfer as donor materials for heterojunction solar cells, *J. Am. Chem. Soc.*, 2006, **128**(10), 3459–3466.
55 K. Rezaeian and H. Khanmohammadi, Naked-eye detection of biologically important anions by a new chromogenic azo-azomethine sensor, *Spectrochim. Acta, Part A*, 2014, **133**, 31–37.
56 M. Odabaşoğlu, *et al.*, Synthesis, spectroscopic characterizations and quantum chemical computational studies of (Z)-4-[(E)-p-tolyldiazenyl]-6-[(2-

hydroxyphenylamino) methylene]-2-methoxycyclohexa-2, 4-dienone, *Spectrochim. Acta, Part A*, 2012, **92**, 357–364.

57 M. Köse, *et al.*, Synthesis, characterization and antimicrobial studies of 2-{(E)-[(2-hydroxy-5-methylphenyl) imino] methyl}-4-[(E)-phenyldiazenyl] phenol as a novel azo-azomethine dye, *J. Mol. Struct.*, 2013, **1053**, 89–99.

58 A. Gözel, *et al.*, Spectral, structural and quantum chemical computational and dissociation constant studies of a novel azo-enamine tautomer, *J. Mol. Struct.*, 2014, **1074**, 449–456.

59 W. Schilf, B. Kamieński and K. Užarević, Nitrogen and carbon CPMAS NMR investigations of keto–enol tautomerism in asymmetric o-hydroxy Schiff bases, *J. Mol. Struct.*, 2013, **1031**, 211–215.

60 N. Nagasundaram, *et al.*, Ultrasound promoted synthesis of new azo fused dihydropyrano [2, 3-c] pyrazole derivatives: In vitro antimicrobial, anticancer, DFT, in silico ADMET and Molecular docking studies, *J. Mol. Struct.*, 2022, **1263**, 133091.

61 C.-H. Li, *et al.*, Design, synthesis, and biological evaluation of dinuclear bismuth (III) complexes with Isoniazid-derived Schiff bases, *J. Inorg. Biochem.*, 2022, **235**, 111931.

62 G. Yali, *et al.*, Comparison of pathogens and antibiotic resistance of burn patients in the burn ICU or in the common burn ward, *Burns*, 2014, **40**(3), 402–407.

63 A. A. Bekhit, *et al.*, Synthesis and biological evaluation of some thiazolyl and thiadiazolyl derivatives of 1H-pyrazole as anti-inflammatory antimicrobial agents, *Eur. J. Med. Chem.*, 2008, **43**(3), 456–463.

64 S. Saravanan and V. Balachandran, Quantum chemical studies, natural bond orbital analysis and thermodynamic function of 2, 5-dichlorophenylisocyanate, *Spectrochim. Acta, Part A*, 2014, **120**, 351–364.

65 M. L. Amin, P-glycoprotein inhibition for optimal drug delivery, *Drug Target Insights*, 2013, **7**, 27–34.

66 P. Politzer and J. S. Murray, Molecular electrostatic potentials and chemical reactivity, *Rev. Comput. Chem.*, 1991, 273–312.

67 P. Politzer and D. G. Truhlar, *Chemical applications of atomic and molecular electrostatic potentials: reactivity, structure, scattering, and energetics of organic, inorganic, and biological systems*, Springer Science & Business Media, 2013.

68 A. May and M. Zacharias, Accounting for global protein deformability during protein–protein and protein–ligand docking, *Biochim. Biophys. Acta, Proteins Proteomics*, 2005, **1754**(1–2), 225–231.

69 M. J. Buehler and Y. C. Yung, Deformation and failure of protein materials in physiologically extreme conditions and disease, *Nat. Mater.*, 2009, **8**(3), 175–188.

70 T. W. Johnson, *et al.*, Reviving B-Factors: retrospective normalized B-factor analysis of c-ros oncogene 1 receptor tyrosine kinase and anaplastic lymphoma kinase L1196M with crizotinib and lorlatinib, *ACS Med. Chem. Lett.*, 2018, **9**(9), 878–883.

71 Z. Sun, *et al.*, Utility of B-factors in protein science: interpreting rigidity, flexibility, and internal motion and engineering thermostability, *Chem. Rev.*, 2019, **119**(3), 1626–1665.

72 M. Rueda, P. Chacón and M. Orozco, Thorough validation of protein normal mode analysis: a comparative study with essential dynamics, *Structure*, 2007, **15**(5), 565–575.

73 Q. R. Johnson, *et al.*, Mapping allostery through computational glycine scanning and correlation analysis of Residue–Residue contacts, *Biochemistry*, 2015, **54**(7), 1534–1541.

74 T. M. Allison, *et al.*, Computational strategies and challenges for using native ion mobility mass spectrometry in biophysics and structural biology, *Anal. Chem.*, 2020, **92**(16), 10872–10880.

75 N. Rawat and P. Biswas, Size, shape, and flexibility of proteins and DNA, *J. Chem. Phys.*, 2009, **131**(16), 51–69.

76 S. Ausaf Ali, *et al.*, A review of methods available to estimate solvent-accessible surface areas of soluble proteins in the folded and unfolded states, *Curr. Protein Pept. Sci.*, 2014, **15**(5), 456–476.

77 S. L. Hilburg, *et al.*, Behavior of protein-inspired synthetic random heteropolymers, *Macromolecules*, 2020, **53**(21), 9187–9199.

78 C. B. Aakeröy and K. R. Seddon, The hydrogen bond and crystal engineering, *Chem. Soc. Rev.*, 1993, **22**(6), 397–407.